NORTHWESTERN UNIVERSITY

Nanofabrication of Transition Metal Chalcogenides and Plasmonic Structures

A DISSERTATION

SUBMITTED TO THE GRADUATE SCHOOL
IN PARTIAL FULFILLMENT OF THE REQUIREMENTS

for the degree

DOCTOR OF PHILOSOPHY

Field of Chemistry

By

Christopher Leo Stender

EVANSTON, ILLINOIS

December 2008

ABSTRACT

Nanofabrication of Transition Metal Chalcogenides and Plasmonic Structures

Christopher Leo Stender

The work described in this dissertation focuses on the development of a general approach to create nanoscale transition metal chalcogenide materials and new methods for controlling architecture of gold pyramidal structures. In the former, we used chemical nanofabrication, a combination of top-down patterning and bottom-up solid-state synthesis, to achieve control over the shape, size, and ordering of the patterned nanomaterials. We demonstrated orientational control over nanocrystals within sub-300 nm patterns of MoS_2 and formed free-standing nanostructures of crystalline NiS_2. In addition, crossed line arrays of mixed metal chalcogenide nanostructures were achieved, and TaS_2 nanopatterns and nanotubes were made by the chemical transformation of tantalum oxide templates. In the latter, a new apparatus was developed for tailoring specific features of the pyramidal structures. We investigated how the optical properties were tuned upon progressively truncating the tip of the pyramids mesostructures affects.

Professor Teri W. Odom
Research Advisor

ACKNOWLEDGEMENTS

I would like to thank all of my colleagues here at Northwestern for helping to make an enjoyable light hearted working environment. I would especially like to thank my advisor Professor Teri Odom for her invaluable tutelage and support during my graduate career at Northwestern University. I would like to thank my other committee members: Professor George Schatz and Professor Michael Wasielewski for their insight and discussions of my research projects during the past 5 years. I would also like to thank my collaborators: Dr. Eric Greyson, Dr. Yelizaveta Babayan, Dr. Jeremy Barton, Warefta Hasan, Dr. Colleen Nehl and Dr. Kevin Shuford for their insight, and valuable contributions to this work. I would like to thank the rest of the Odom group and my friends from around Northwestern for discussion and helping to add to the great research environment here.

I need to thank Mr Thomas Lowe for really sparking my interesting in chemistry in high school. Having taught all of my older siblings he was already quite experienced with methods necessary to pique the Stender kids' interest. Early in the first semester he preformed a thermite reaction with me sitting particularly close. While not scorched physically an impression was made none the less. That impression nearly a decade later encouraged me to return to school and pursue a degree in chemistry.

I would like to thank all the professors at Linfield College where I received my undergraduate degree. I would like to especially thank, Professor Thomas Reinert for advising me throughout my undergraduate life and for helping to create such a great department, Professor Brain Gilbert for help us to restart the chemistry club and being our faculty advisor, and Professor Robert Wolcott for their support and discussions throughout my time at Linfield.

Many thanks to Professor Elizabeth Atkinson for giving me my first real taste of research and fostering some of the creativity required to be successful at research. In my project I examined the methods and strategies for creating dye-sensitized solar cells.

One of the greatest things that have happened during my time at Northwestern was finding my wife Tammara Stender. I would like thank her for her support, love and understanding over the last few years. She has been an amazing partner in every aspect of life and I am grateful for her in my life. Her family has been amazingly welcoming from the start and many fun holidays have been spent in their company.

I would also like to say thanks to friends and family back home for not telling me that I was completely crazy for going back to school to completely change my career path knowing that it would take the better part of a decade to accomplish. A special thank you to my parents, Robert and Sharon Stender, for always helping us to believe that anything is possible if you put your mind to it, and instilling the stubborn determination to never give up.

Without the support of my friends and family I am not sure if I would have made it this far. It has been a long and winding road with night classes after work at Clark College to quitting my job to return to full time school at Linfield College and finally ending up here at Northwestern University. Although the learning road never ends, it is the end of this capture of my academic life. I'm looking forward to the low stress pottery class in the future. I would like to dedicate this thesis to everyone who helped make it possible and especially my wife Tammara Stender and my family.

CLS
Evanston, IL
December 2008

To my wife Tammara Stender and our son or daughter to be born around April 2009

to my parents, Robert and Sharon Stender

my siblings, Kim, Mark and Ann Stender

and

the rest of my family

TABLE OF CONTENTS

Abstract …… 3

Acknowledgements …….. 4

List of Illustrations …….. 11

List of Common Abbreviations …….. 13

Chapter 1 Introduction 15

1.1 General Overview 16

1.2 Goals and Organization of Thesis 17

Chapter 2 Tools for Characterization and Fabrication of Patterned and Free-Standing Nano/Meso Structures 19

2.1 Introduction 20

2.2 Analytical X-ray and Electron Techniques 21

2.2.1 X-ray Diffractometry 21

2.2.2 X-ray Photoelectron Spectrometry 21

2.2.3 Energy Dispersive X-ray Spectroscopy 24

2.2.4 Scanning Electron Microscopy 24

2.3 Single Particle Optical Spectroscopy 27

2.4 Overview of Lithography 30

2.4.1 Materials 30

2.4.2 Fabrication of Masters and PDMS Mask for Phase-Shifting Photolithography (PSP) 31

2.4.3 Fabrication of PSP Dot Masters 33

2.4.4 Fabrication of Metal Nanopatterns for Chemical Conversions Reactions 35

2.5 Summary 38

Chapter 3 Confined Crystal Growth using MoS_2 as a Model System 39

3.1 Introduction 40

3.2 Experimental Methods and Discussion 41

3.2.1 Oxidation State Characterization of Precursor Mo Film 42

3.2.2 Generation of Mo Patterned Structures and Chemical Conversion to MoS_2 42

3.2.3 Structural Characterization of Patterned and Thin Films of MoS_2 44

3.2.4 Optical Characterization and Empirical Formula Determination of Thin Film MoS_2 50

3.3 Conclusions 53

Chapter 4 Chemical nanofabrication 54

4.1 Introduction 55

4.2 Experimental Methods and Discussion 56

4.2.1 Fabrication of Ni Patterned Structures and Chemical Conversion to NiS_2 59

4.2.2 Structural Characterization of Patterned NiS_2 61

4.2.3 Fabrication and Structural Characterization of Patterned Ag_2Se 63

4.2.4 Fabrication and Elemental Analysis of Patterned NiS_2/Ag_2Se Heterogeneous Arrays 63

4.2.5 Generation of Free-Standing NiS_2 Structures 65

4.3 Conclusions 68

Chapter 5 Solid State Chemistry of TaS_2 Nanostructures 70

5.1 Introduction 71

5.2 Experimental Methods and Discussion 73

5.2.1 Fabrication of Patterned Ta Lines on Fused Silica 74

5.2.2 Investigation and Analysis of Temperature Effects on the Crystal Structure of Ta_2O_5 75

5.2.3 Chemical Conversion of Ta_2O_5 Amorphous Nanowires to TaS_2 Nanowires 75

5.2.4 Chemical Conversion of Ta_2O_5 Nanotubes to TaS_2 Fullerene-like Nanotubes 78

5.3 Conclusions 81

Chapter 6 Optical Properties of Tipless Pyramids 83

6.1 Introduction 84

6.2 Experimental Methods and Discussion 85

6.2.1 Fabrication of Tipless Pyramids 86

6.2.2 Optical Characterization of Tipless Pyramids 88

6.3 Conclusions 97

References 98

Appendix 1 LA/CVD Furnace Construction 106

Appendix 2 Tilting Rotational Stage 109

LIST OF ILLUSTRATIONS

Figure 2.2.1	Schematic diagram of an X-ray diffractometer ..…….……..	22
Figure 2.2.2	Schematic diagram of an XPS ……...……..	23
Figure 2.2.3	EDS spectrum of MoS_2 film……....	25
Figure 2.2.4	SEM image of NiS_2 rings……....	26
Figure 2.3.1	Microscope-spectrometer setup for single particle spectroscopy……..	28
Figure 2.4.2	Fabrication scheme for PSP masters and PMDS stamps……..…….	32
Figure 2.4.3	Fabrication scheme for photoresist dot masters and PDMS dot masks.....	34
Figure 2.4.4.1	Fabrication scheme for patterning arbitrarily shaped metal nanostructures…….	36
Figure 2.4.4.2	Fabrication scheme for dot and parallelogram etch masks….……....	37
Figure 3.2.2	XPS analysis of Mo films…….……..	43
Figure 3.2.3	Fabrication scheme for generating MoS_2 nanostructures..…….	45
Figure 3.2.4.1	SEM examination of MoS_2 nanocrystal orientation……...……	46
Figure 3.2.4.2	Illustration of patterning TMC flexibility..……...…….	48
Figure 3.2.4.3	X-ray diffraction of oriented MoS_2 nanocrystals……..…….	49
Figure 3.2.5.1	Optical characterization of MoS_2 films……..	51
Figure 3.2.5.2	XPS characterization of MoS_2 films……..……	52
Figure 4.2.2	Schematic outline for patterning arbitrary TMC materials...…….	58
Figure 4.2.3	XPS analysis on 400 nm spaced NiS_2 lines……...…….	60
Figure 4.2.4	SEM and GXRD analysis of NiS_2 patterned structures……...……..	62
Figure 4.2.5	SEM and GXRD analysis of Ag_2Se patterned lines...…….……..	65

Figure 4.2.6	SEM analysis of crossed heterogeneous arrays of NiS_2/Ag_2Se lines……	66
Figure 4.2.7	Schematic outline and SEM examination for generating free-standing NiS_2 parallelograms……	67
Figure 5.2.3	SEM and GXRD analysis of temperature dependent structural changes in patterned Ta_2O_5 lines…..……....	76
Figure 5.2.4	SEM and GXRD analysis of patterned TaS_2 lines..……....	77
Figure 5.2.5.1	GXRD analysis and conversion dynamics of Ta_2O_5 nanotubes to TaS_2 IF……	79
Figure 5.2.5.2	XPS analysis of conversion dynamics of Ta_2O_5 nanotubes to TaS_2 IF…..	80
Figure 6.2.2.1	Schematic of tilting rotational stage and resulting structures……	87
Figure 6.2.2.2	Demonstration of the flexibility in size control of TL…….….	89
Figure 6.2.2.3	Summary of theoretical structural expectations for TL for various parameter changes…….…….	90
Figure 6.2.3.1	Optical trends for TL……..	91
Figure 6.2.3.2	Refractive index sensitivity study of TL……..……...…...	93
Figure 6.2.3.3	Refractive index sensitivity study of square based WT...……..	94
Table 6.2.3	Summary of FOM for square based TL and WT..…….	96
Figure A1	Diagram of laser ablation/CVD furnace…….	108
Figure A2	Diagram of Tilting Rotational Stage……..	110

LIST OF COMMON ABBREVIATIONS

2D – two-dimensional

3D – three-dimensional

AFM – atomic force microscope

APD – avalanche photodiode

BSE – backscattered electrons

CCD – charge coupled device

CDW – charge density wave

DF – dark-field

DI – deionized water

E-beam – electron beam

EBL – electron beam lithography

EDS – energy dispersive X-ray spectroscopy

EM – electromagnetic

FL – focal length

FWHM – full width half max

GXRD – glancing angle X-ray diffraction

IF – inorganic fullerene-like nanotubes

IPA – isopropyl alcohol

ITO – Indium tin oxide

LN_2 – liquid nitrogen

LSPR – localized surface plasmon resonance

NA – numerical aperture

NC – nanocrystals

NP – nanoparticle

NT – nanotube

PDMS – polydimethylsiloxane

PSP – phase-shifting photolithography

QD – quantum dots

SC – spectral coverage

sccm – standard cubic centimeter per minute

SE – secondary electron

SEM – scanning electron microscope

SG – space group

S/N – signal-to-noise

SP – surface plasmon

SPP – surface plasmon polariton

SPS – single particle scattering spectroscopy

SR – spectral resolution

TEM – transmission electron microscope

TMC – transition metal chalcogenide

TP – tipless pyramids

UV – ultraviolet

XPS – X-ray photoelectron spectroscopy

Chapter 1

Introduction

1.1 General Overview

Since the original concept of the transistor by Julius Lilienfeld in 1925 there has been a steady progression in the size reduction of the device that lead to modern day computers. With smaller structures, there is an increased challenge for controlling architecture and placement on substrates. Without precise management over the positioning of components the modern computer would not function. Nanoscale materials and structures exhibit interesting and useful optical, electronic and physical properties for diodes, photodetectors, and chemical sensors.[1-3] There are two complementary strategies for organizing nanostructures on surfaces: (i) synthesizing the nanomaterials and then assembling them into useful architectures or (ii) growing the nanostructures directly at pre-defined locations. The former approach relies on assembly methods such as fluidic-based assembly,[4, 5] electric and magnetic field mediated assembly,[6-8] electrostatic assembly,[9, 10] and template-based assembly.[11, 12]

The construction of nanoscale devices relies on distributing preformed nanostructures onto a substrate, locating them in a scanning electron microscope and then attaching electrodes to the nanostructure. It is more desirable to have well-defined locations of nanostructures to facilitate device construction for two reasons: (i) the elimination of an assembly step after the growth of nanomaterials, and (ii) and the arrangement of nanostructures on surfaces with a high level of precision. Assembly and generation of nanostructures has been achieved using a variety of serial tools such as focused ion beam milling (FIB), electron beam lithography (EBL), dip-pen nanolithography (DPN), and photolithography. Serial methods such as EBL and FIB can generate feature down to about 20 nm and have the flexibility to pattern arbitrary shapes.[13, 14] While both methods offer shape and pattern flexibility, they have the drawback of being

inherently serial methods that are only able to pattern small areas (100 μm^2).[15-17] Advances in DPN have resulted in arrays of probes with 55,000 tips capable of patterning identical organic ink structures.[18] Even with these improvements, the technique remains a slow serial process for placement and generation of nanostructures. Serial methods are not scalable in any industrial sense and remain expensive methods for generating patterned nanostructures. Nanosphere lithography and laser-assisted embossing can also generate sub-100 nm patterns in metals and semiconductors, and in a parallel manner. These patterns, however, are limited to simple geometries (hexagonally closed packed or honeycomb structures).[19, 20]

The preferred method for nanostructure generation and assembly is a parallel approach, such as photolithography, where identical features can be patterned simultaneously. Unfortunately, standard photolithography is limited by the diffraction limit of the wavelength of light ($\lambda/2$), and is difficult to achieve structures much below 400 nm. Phase-shifting photolithography (PSP) is a parallel fabrication method that takes advantage of the refractive index differences at the polymer/air interface of the patterned PDMS stamp and causes a node of zero light penetration in the near-field capable of generating structures down to ~30 nm.[21, 22] These techniques have been used to create nanostructures of Si and GaAs by chemical etching[23, 24] and to direct the growth of arrays ZnO nanowires and carbon nanotubes.[25-27]

1.3 Goals and Organization of Thesis

The goals of this thesis are to develop new methods for generating and understanding confined crystal growth and to examine how architecture of mesostructures (100-1000 nm) affects optical properties. Chapter 2 describes the instrumentation used for X-ray, electron beam

analysis and far-field spectroscopic studies of both patterned and free-standing nanostructures. This chapter also introduces lithographic techniques used for generating the various structures in the remainder of the thesis. Chapter 3 discusses our development of new techniques for patterning and growing functional transition metal chalcogenide (TMC) structures of MoS_2. This chapter highlights improvements for patterning and growth of TMC materials on substrates. Chapter 4 expands our capabilities of patterning TMC materials to include chemically converted free-standing mesostructures and heterogeneous arrays of different TMC materials. Such heterogeneous arrays would not be possible using standard lithographic methods. Chapter 5 shows the extension of the method to include high temperature refractory metals, specifically Ta. This chapter also includes how to generate TMC inorganic fullerene-like nanotubes from amorphous Ta_2O_5 nanotubes. Finally, chapter 6 examines how structure affects the optical properties of anisotropic, tipless pyramidal particles.

Chapter 2

Tools for Characterization and Fabrication of Patterned and Free-Standing Nano/Meso Structures

2.1 Introduction

Advances in nanofabrication have enabled generation of mesoscale (100-1000 nm) and nanoscale (1-100 nm) structures that exhibit interesting optical, electronic and crystal growth dynamics. The growth of patterned crystalline nanostructures and characterization on substrates remains challenging because of the limited synthetic techniques for growing crystals on patterned surfaces, and the small sample amounts and for characterization.

Electrons and x-ray photons are two probe sources for nanocrystal characterization. We have used transmission electron microscopy (TEM), electron energy loss spectroscopy (EELS), selected area electron diffraction (SAED), energy dispersive X-ray spectroscopy (EDS), scanning electron microscopy (SEM), glancing angle X-ray diffraction (GXRD), and X-ray to photoelectron spectroscopy (XPS) to characterize our nanopatterned substrates.

X-ray and electron beam analytical techniques are ideal for crystalline nanostructures; however, examinations of polycrystalline noble metal structures require other tools for characterization of physical properties. Probing the opto-electronic properties of arrays and single nanostructures has been accomplished using UV-vis spectroscopy to probe the electronic transitions of the crystal structure or element being examined. Metallic single free-standing nanostructures are most commonly probed by a method that examines the light scattered off the nanostructures surface. The scattered light carries information related to the plasmonic interactions on the surface of the particle and has been used to great extend in recent years for various sensing applications.[28-32] Each set of techniques have their own advantages and disadvantages, but taken as a whole can give a complete picture of physical properties, determine empirical formulas, and probe electronic states of structures and arrays.

2.2 Analytical X-ray and Electron Techniques

2.2.1 X-ray Diffractometry

Crystalline, polycrystalline and nanocrystalline structures all have repeating unit cells and long range ordering that are unique signatures of compounds. In our studies, we used GXRD and its applications for structural analysis of patterned nanostructures on Si (100) substrates. GXRD is useful technique for analyzing thin films and nanostructures on substrate because the geometry can be adjusted such that the X-ray beam will not penetrate the underlying substrate (Si) yet will still provide structural information about the thin film or patterned nanostructures. Figure 2.2.1A illustrates a typical x-ray diffractometer with the inset demonstrating Bragg's Law conditions for constructive interference. Figure 2.2.1B shows a sample diffraction spectrum of patterned 3R-MoS_2 lines spaced by 2 μm.

2.2.2 X-ray Photoelectron Spectrometer

To supplement GXRD analysis, XPS was used. XPS is a technique that utilizes the photoelectric effect to determine elemental composition and empirical formulas of the nanomaterials. The technique is widely versatile on substances from inorganic compounds to glue and biomaterials and is considered a nondestructive analytical technique to most materials. Although the penetration depth of the X-ray beam is on the order of several microns, only electrons excited in the first ~10 nm are ejected because electrons deeper within the material are recaptured or trapped. The XPS used for our work has a monochromatic light source and a spectral resolution of ~0.25 eV. Quantitative analysis of atomic percentages is

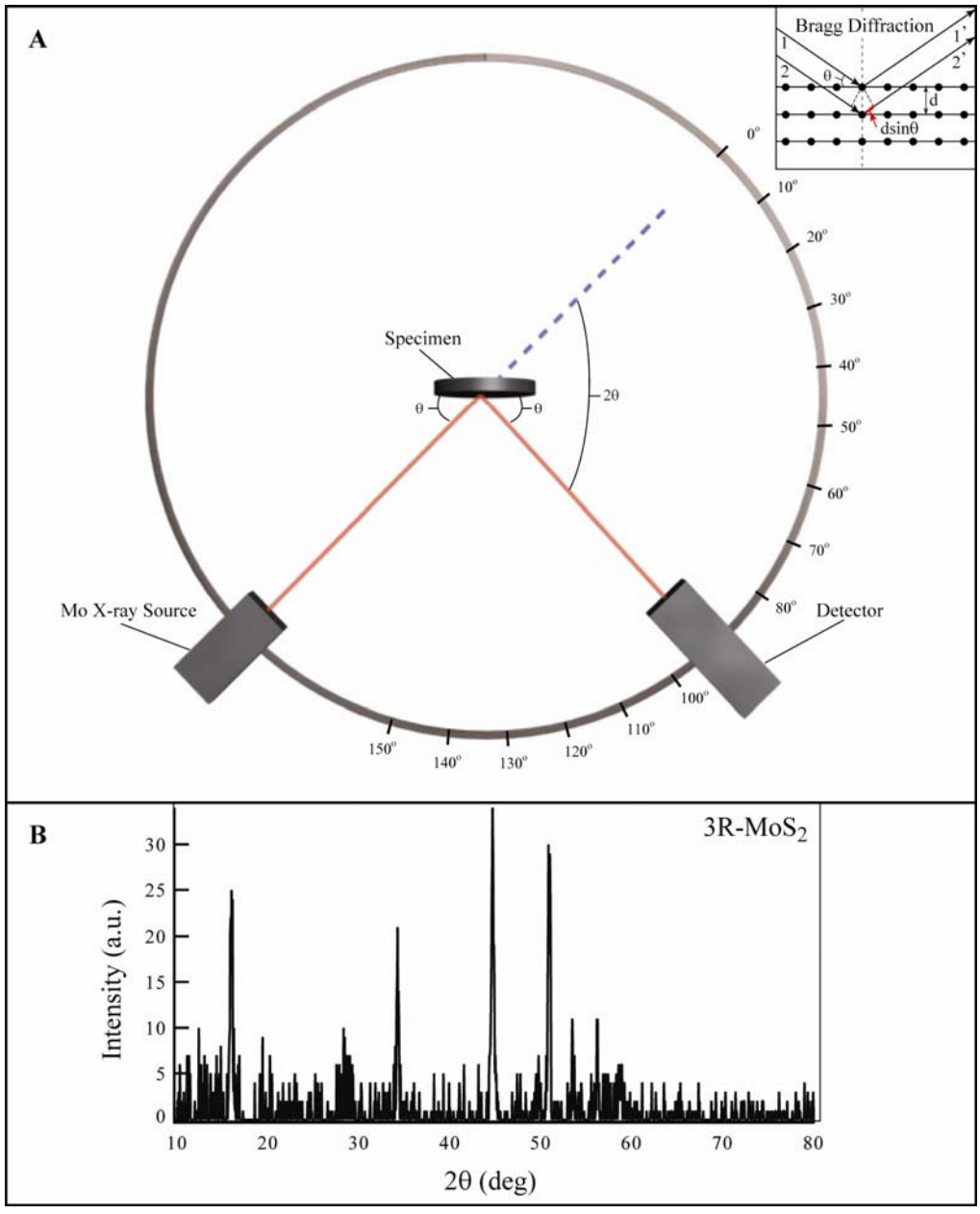

Figure 2.2.1. A) Schematic Diagram of x-ray Diffractometer. Inset Bragg's Law conditions. B) Diffraction pattern of 2 μm spaced 3R-MoS_2 lines

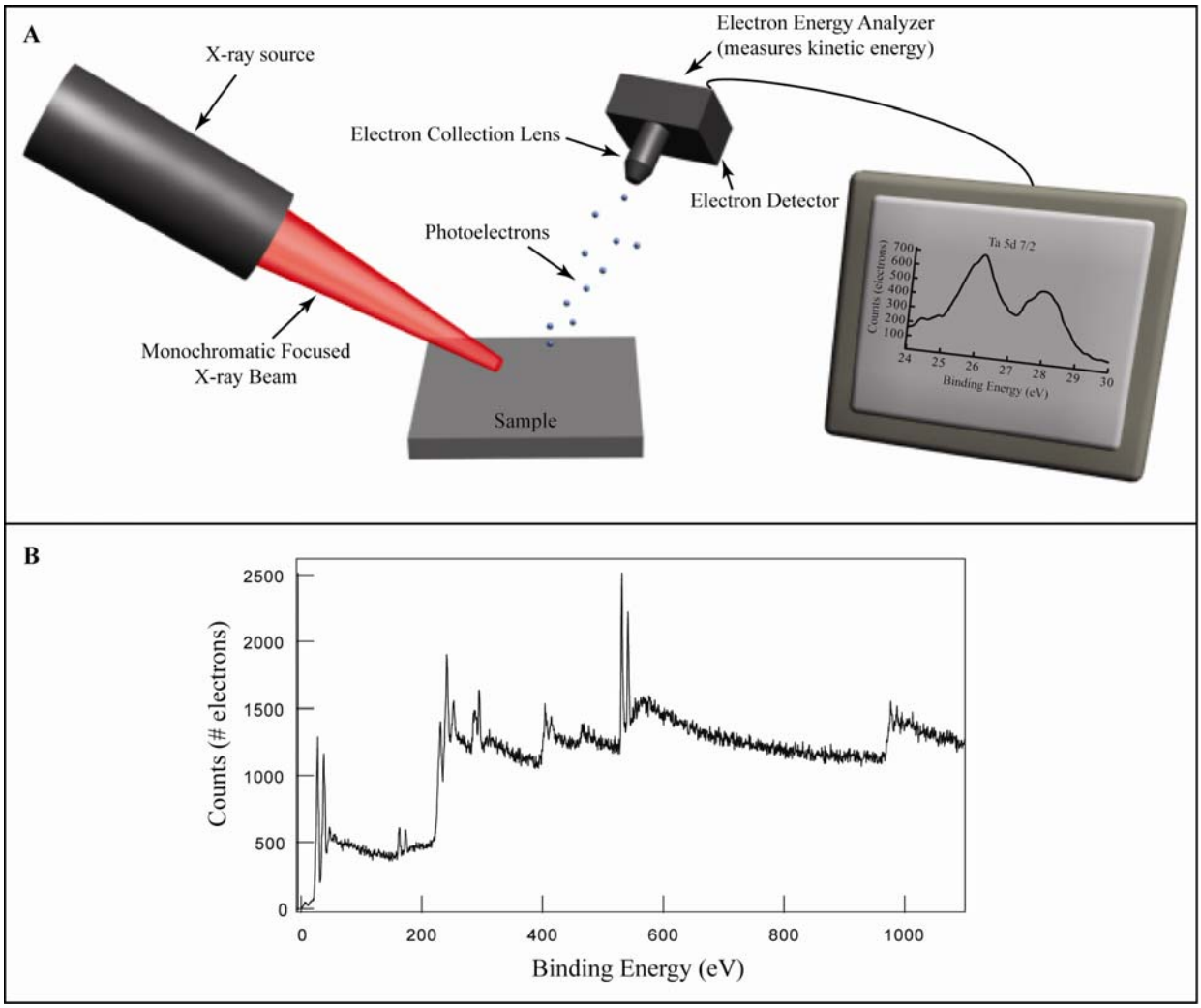

Figure 2.2.2. A) Schematic diagram of an XPS with inset showing characteristic Ta peaks. B) Full TaS_2 nanotube XPS spectrum.

challenging using photoelectrons because of the small sample quantity relative to the underlying substrate. Taking this difficulty into account, the XPS analysis was used only to determine oxidation states for the nanostructures studied. Figure 2.2.2A shows a diagram of a typical XPS setup and 2.2.2B displays sample spectra from TaS_2 nanotubes on Si.[33]

2.2.3 Energy Dispersive X-ray Spectroscopy

EDS was used to verify the elemental content of the Ag_2Se/NiS_2 crossed heterogeneous arrays. Similar to XPS, EDS uses the characteristic X-rays emitted from an atom that has had an inner shell electron ejected by a high energy charged particle beam and an outer shell electron relaxes to fill the hole. Because all elements have a unique electronic structure the X-ray emitted through this process provides a characteristic signature used for elemental identification. There are some difficulties associated with this method, however, namely that several elements have overlapping peaks, which make making it difficult or impossible to deconvolute spectra.[34] Figure 2.2.3 shows a typical EDS spectrum from a MoS_2 thin film. The spectrum illustrates the overlapping of the S and Mo characteristic peaks at ~2.3 eV.

2.2.4 Scanning Electron Microscopy

Throughout this work, high resolution LEO 1525 SEM with a Schottky thermal emission gun with upper and lower SE detectors was used to examine the morphology and locations of patterned and free-standing nanostructures. The LEO 1525 is capable of high-resolution (<10 nm). Figure 2.2.4 shows an SEM image taken at a tilt angle of 45° of NiS_2 rings on a raised Si template.

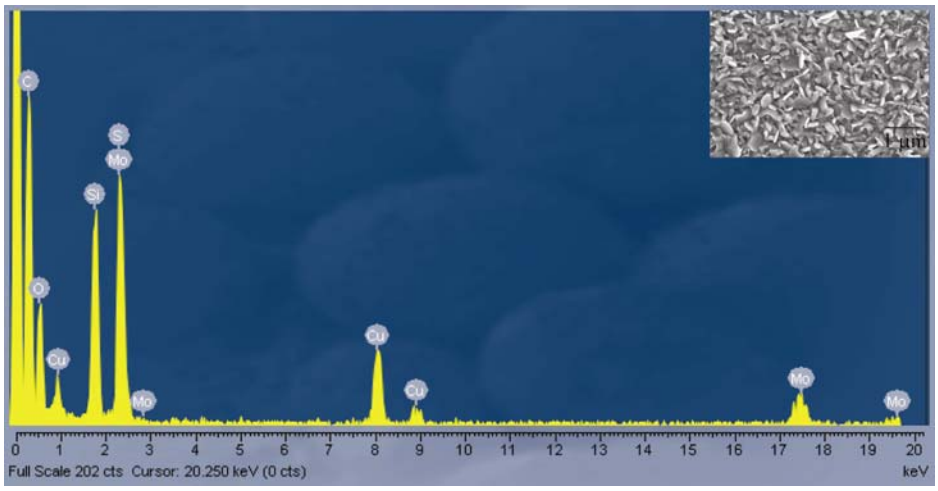

Figure 2.2.3. EDS spectrum of 90 nm thick MoS_2 film (inset)

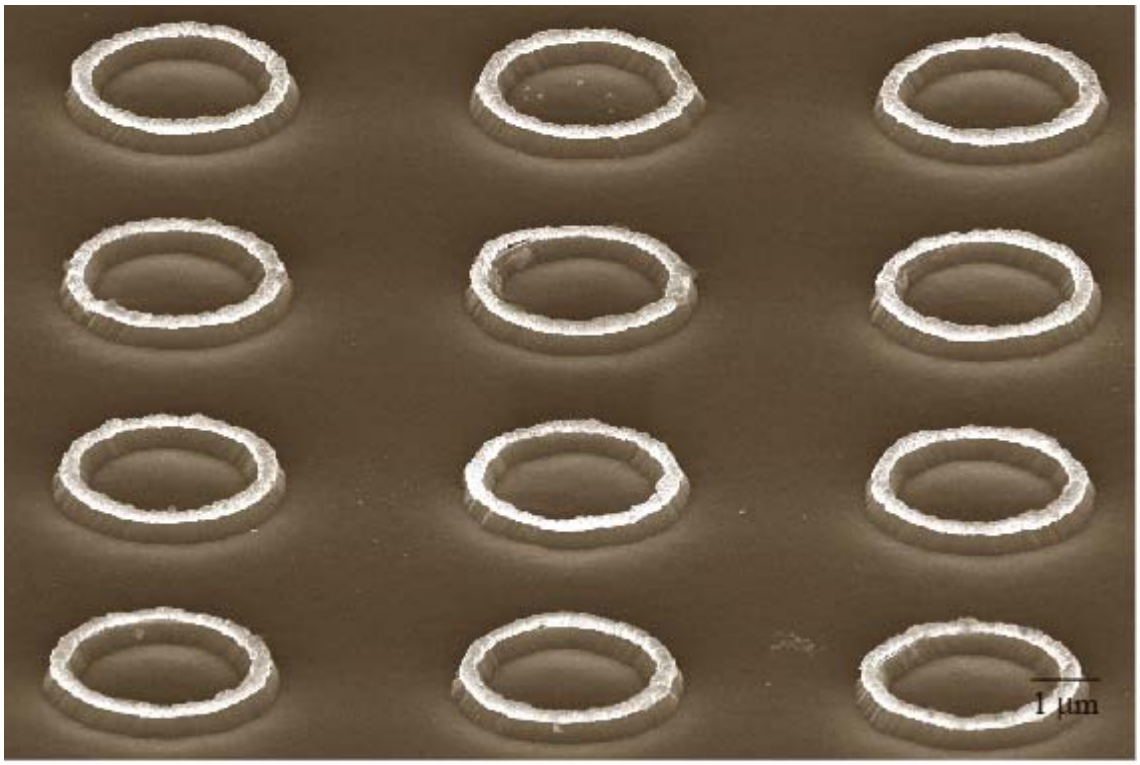

Figure 2.2.4. SEM image taken at 45° tilt of NiS_2 rings on top of raised Si rings.

2.3 Overview of Single Particle Optical Spectroscopy

Optical properties of nanoparticles (NPs) depend on material, size and shape of the structures.[35] Originally, NPs were only able to be studied while in large arrays; however, recent advances have enabled optical studies of single nanostructures.[36, 37] SPS allowed us to investigate the effects of subtle architectural changes on the optical properties of our pyramidal structures, namely the progressive truncation of the particle tips.

Single particle dark-field scattering spectroscopy of tipless pyramids (TL) was performed on a Nikon TE2000 inverted microscope coupled to a 550 mm focal length (*f*) imaging Triax 552 spectrometer with *f* =10 cm convex lens. Figure 2.3.1A provides a schematic representation of our SPS setup. Figure 2.3.1B shows a typical spectrum after background subtraction and normalization of a θ=50° tipless pyramid (TL). The Triax 552 has two exit and entrance ports enabling multiple source signals and detectors and is fitted with two LN_2 cooled charge coupled device (CCD) detectors: one near-infrared (NIR) detector (1024x1, InGaAs, Jobin Yvon)) and one VIS imaging detector (1024x256, Symphony, Jobin Yvon). A CoolSnap ES video camera by Photometrics was added to aid in identifying and aligning the nanoparticle.

The light is routed through the exit port of the microscope to the spectrometer and separated by a distance of 40 cm with a convex lens (*f*=10 cm) positioned at 20 cm from the spectrometer. According to the lens equation:

$$\frac{1}{S_1}+\frac{1}{S_2}=\frac{1}{f}$$

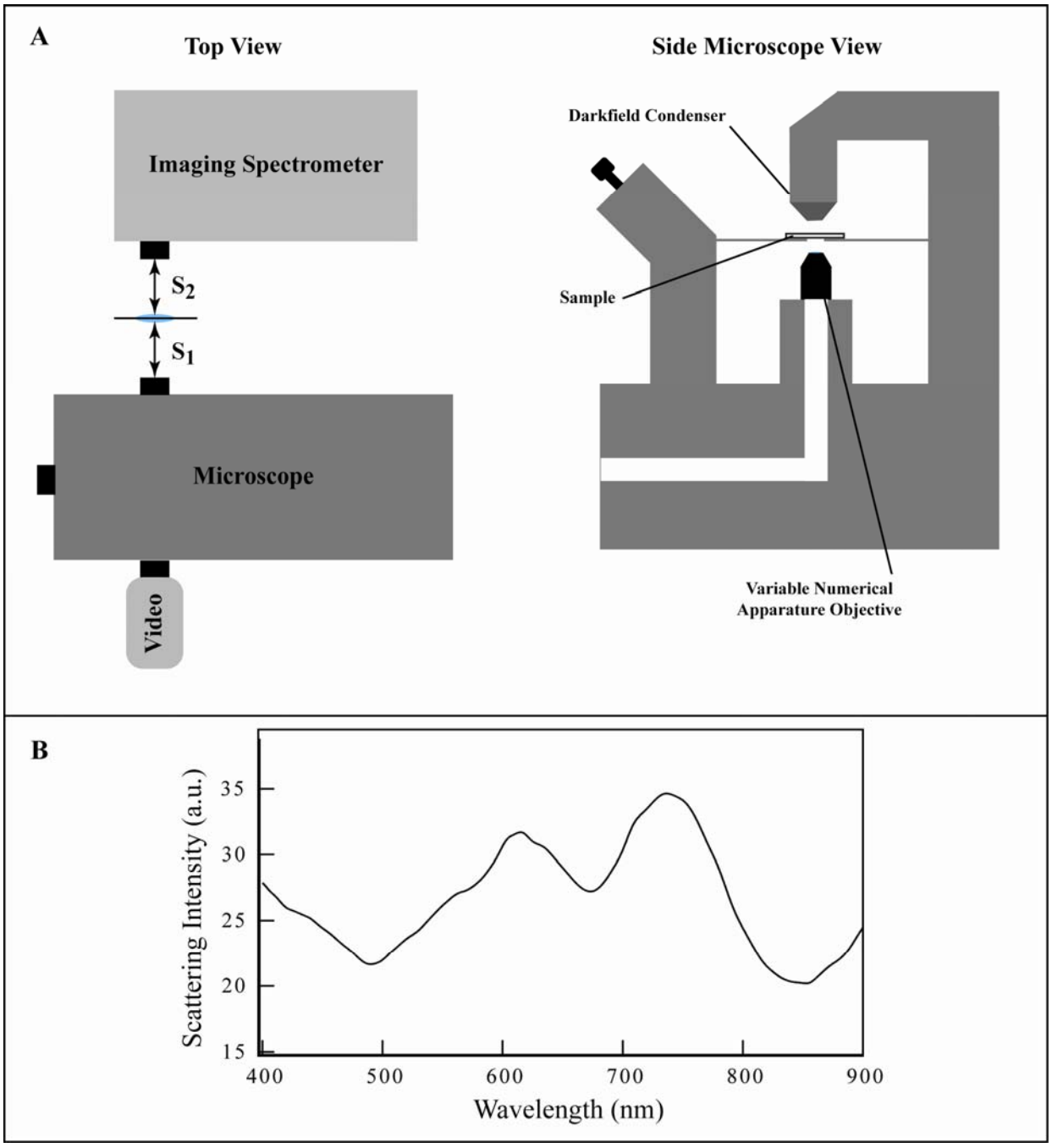

Figure 2.3.1. A) Schematic diagrams of single particle scattering spectroscopy setup. B) Typical θ=50° TL spectrum, entrance slit width 1 mm and exit slit width 0.6 mm to isolate the particle.

where *f* is the focal length of the lens, S_1 is the distance from the microscope exit port to the lens and S_2 is the distance from the lens to the spectrometer entrance port, changing the location of the lens causes the image on the CCD to be magnified or demagnified; if $S_1=S_2$, the image is not magnified on the CCD.

The nanoparticles were drop coated onto a numerically annotated grid on ITO coated glass and allowed to settle for 15 min. The substrate was then blown dry with N_2 to avoid any salt crystallizing during the slow air drying process. The sample was placed on an inverted microscope and illuminated with light from a halogen tungsten bulb through a dark field (DF) condenser (numerical aperture (NA)=0.80-0.95). An oil immersion variable aperture (NA 0.5-1.3) 100X was situated below the sample to collect the scattered light from the nanoparticles. The entrance slit was set to 0.6 mm with an exit slit width of 1.0 mm. The grating was set to zero order position to project an image of a single TL onto the CCD. A video camera was used to correlate the location of the particle from the SEM image with its projection on the VIS CCD detector. The NA on the collection lens was set to be lower than that of the DF condenser lens such that only the scattered light would be collected. The spectrometer grating was then set to disperse the first order diffracted light onto the CCD, and the nanoparticle spectrum was acquired over 2000 msec. The background spectrum was taken under the same parameters from an open space near the nanoparticle to ensure accurate background spectra for subtraction. Next, the lamp profile was obtained by increasing the NA of the objective lens to 1.3 for collection of the transmitted light for 20 msec. The raw spectra were processed by removing the background scattering and correcting for the lamp spectral profile and CCD efficiency with the following formula:

$$NS = \frac{SP - SB}{SL}$$

where *NS* is the normalized scattering, *SP* is the raw particle, *SB* is the background, and *SL* is the lamp profile spectra.

2.4 Overview of Lithography

Photolithography requires a mask to be placed between the light source and the substrate. Conventional photolithography uses a plate of quartz with patterned Cr features. In contrast PSP uses an elastomeric polydimethylsiloxane (PDMS) phase-shifting mask that is placed into conformal contact with the photoresist. We used variations of PSP to generate our micro and mesoscale structures.

2.4.1 Materials

Photolithography: Negative tone-resist, Micro Resist Technology ma-405, positive tone-resist, Shipley 1805, and resist developers LDD^{TM}-26W (for ma-405) and Microposit 351 (for Shipley 1805) were purchased from MicroChem. LDD^{TM}-26W was used as received and Microposit 351 was diluted with deionized water (1:5). Photoresist remover 1165 was purchased from MicroChem. 4-methyl-2-pentanone (Sigma-Aldrich) was used to dilute ma-405. Fluorosilane ((tridecafluoro-1,1,2,2-tetrahydrooctyl trichlorosilane) was purchased from Gelest and used for silanizing photoresist masters on silicon substrates.

Masks: PDMS prepolymer kit (Sylgard 184) for preparing soft (*s*-) PDMS was purchased from Fisher Scientific. We purchased the components of hard (*h*-) PDMS from Gelest. To prepare *h*-PDMS, first 3.4 g VDT-731 ((7.0-8.0% vinylmethylsiloxane)-dimethylsiloxane copolymer,

trimethylsolixy terminated, 800-1,200 cSt), 8-20 μL Pt-catalyst (platinum-divinyl tetramethyl-disolixane complex in xylene, SIP6831.1, 2.1-2.4% Pt) where mixed thoroughly. Then, 1 drop modulator from an 18 gauge needle (2,4,6,8-tetramethyl-2,4,6,8-tetravinylcyclotetrasiloxane) was added and combined. Last, 1 g HMS-301 ((25-30% methylhydrosiloxane)-(dimethylsiloxane) 25-35 cSt) was inserted followed by application onto patterned wafer.

Substrates: Si (100) 3", P/B doped, 1-10 Ω-cm, 381 ± 50 μm, test grade wafers were purchased from Silicon Quest International. Indium tin oxide (ITO) (150 nm) coated glass slides (0.4 mm) were purchased from Thin Film Devices.

Chalcogenide Precursor Materials: Mo, Ti, Cr, Ta, Ni and Ag e-beam materials were purchased from Kurt J. Lesker with purities >99.9%. Carrier (Ar) and reaction gases (H_2S) were purchased from AirGas and Matheson Tri Gas.

2.4.2 Fabrication of Masters and PDMS Mask for Phases-Shifting Photolithography

Figure 2.4.2 illustrates the procedure involved in fabricating photoresist masters and PDMS masks for PSP. Positive-tone photoresist, (Shipley 1805) was spin-cast onto a Si (100) wafer at 4000 rpm and baked on a temperature programmable hotplate at 105 °C for 4 min. The wafer was brought into contact with a Cr patterned quartz masks with the desired features (lines or circles of various spacings and sizes) and exposed to broadband UV light (~14 mW/cm^2) using a Quintel 2000 mask aligner for several seconds. The mask was then removed and the

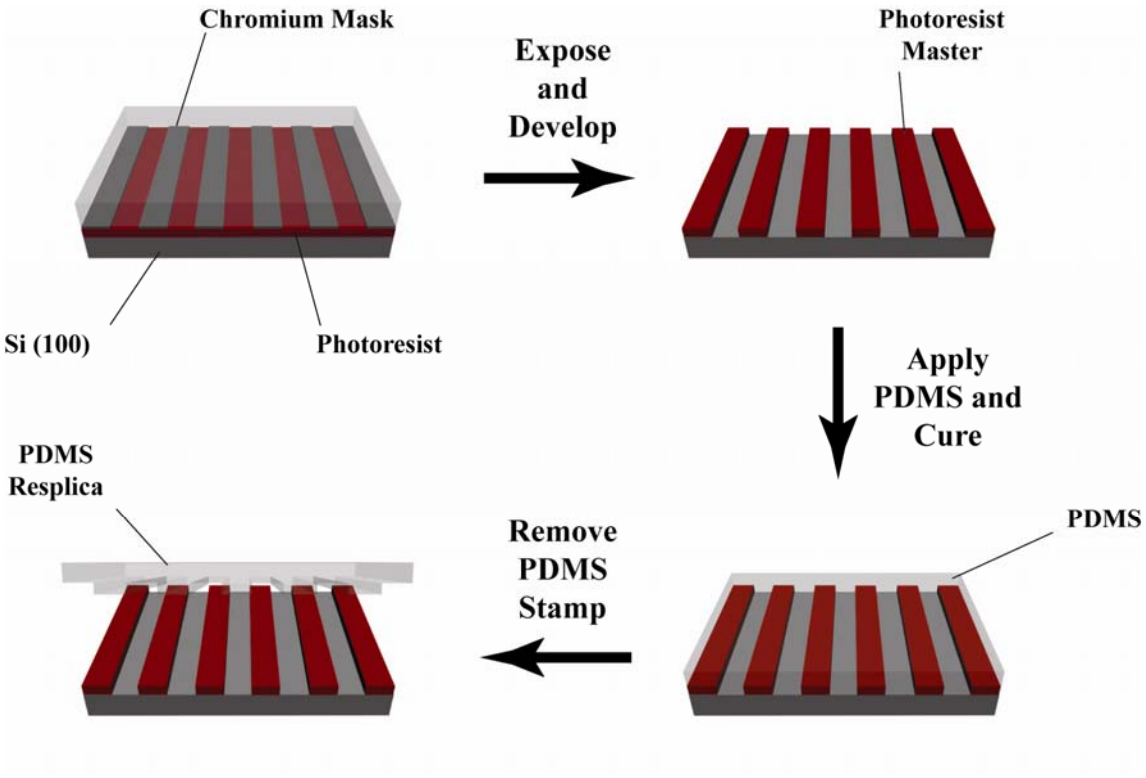

Figure 2.4.2. Fabrication schematic for generating PSP masks.

wafer was developed in a diluted solution of Microposit 351 to reveal the structures with the same spacing and architecture as the Cr mask.

The elastomeric phase masks were prepared by molding and curing PDMS against photoresist masters with patterned features. First, however, the masters were functionalized with a silane monomer to prevent PDMS adhesion to the Si substrate by placing the patterned wafer and a few drops of fluorosilane into a vacuum desiccator for 3 h. A composite *h* and *s*-PDMS stamp was prepared by first spin coating *h*-PDMS onto the master, followed by curing for 2 min at 70 °C. Then 3 mm of *s*-PDMS was poured onto the *h*-PDMS and cured for 4 h at 70°C.

2.4.3 Fabrication of PSP Dot Master

Fabrication of masters with arrays of dots was prepared by molding PDMS to photoresist posts made using PSP line masks (Figure 2.4.3). First, positive-tone photoresist was spun onto Si (100) wafers at 4000 rpm and cured for 4 min at 105 °C. The PDMS line mask was then placed into conformal contact with the photoresist and exposed for several seconds to broadband UV light. The mask was then removed, rotated 90° and reapplied to the photoresist. After an additional exposure to UV light, the wafer was then developed in dilute Microposit 351 to reveal small (<250 nm) posts. Posts were created at the intersections of the two line patterns that were rotated 90° relative to each other. After development, the patterned wafer was placed into an oxygen plasma chamber to clean off residual photoresist. The cleaned patterned stamp was then placed into a vacuum desiccator in the presence of fluorosilane for 3 h. After application of the protective silane layer, *h*-PDMS was spun onto the wafer and cured at 70 °C for 2 min followed by application of 3 mm PDMS and further curing for 3 h at 70 °C. The resulting PDMS stamp

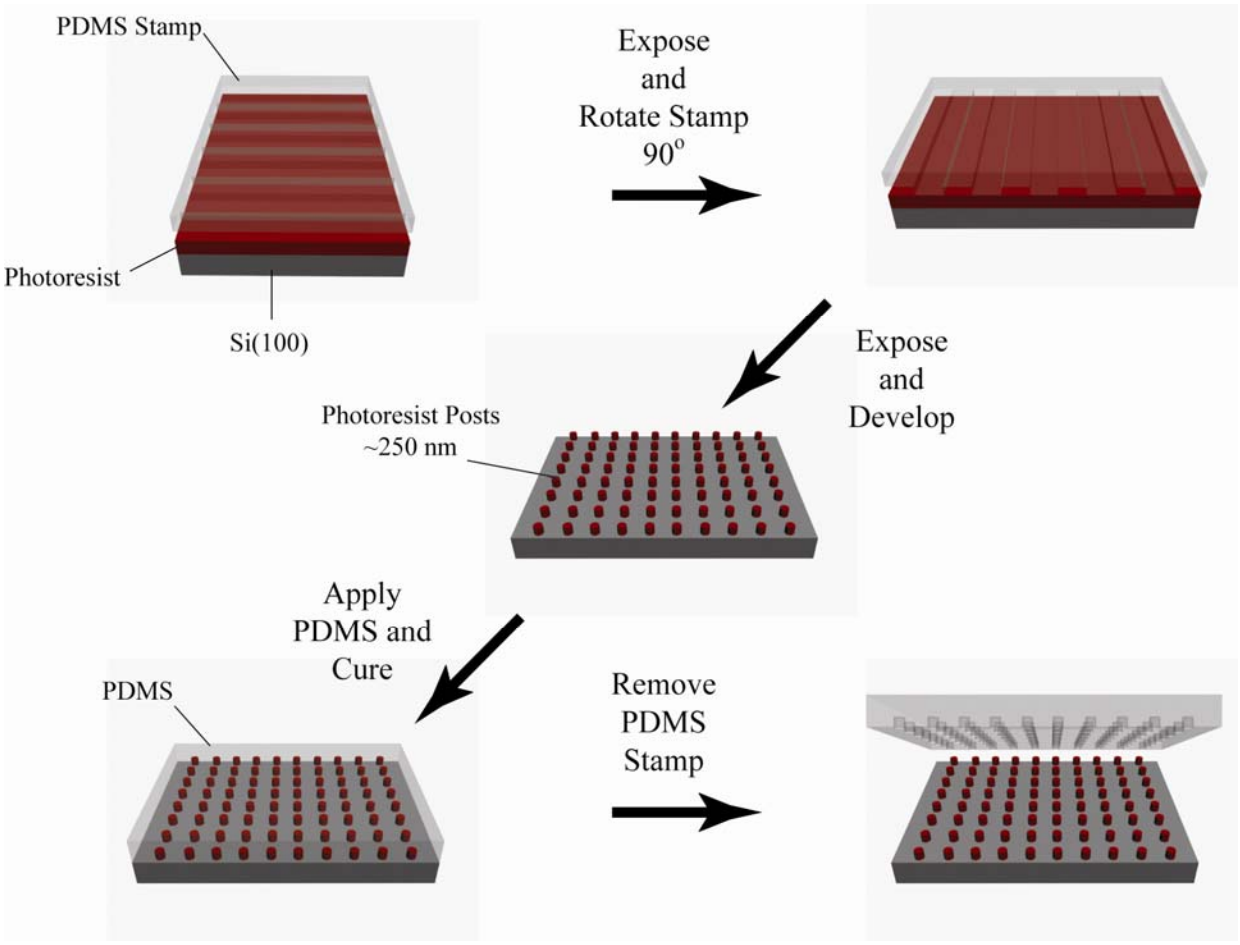

Figure 2.4.3. Fabrication scheme for generating PDMS dot masks. First, PSP is used to expose a line pattern followed by rotation of the mask 90°, exposure and development. PDMS is then cured on the patterned posts and the stamp is removed.

was patterned with ~250 nm recessed pits spaced by 2 μm. Unlike the more robust conventional photolighographically generated master can survive for many replications, dot masters are used only once to make a mold that can last several months.

2.4.4 Fabrication of Metal Nanopatterns for Chemical Conversion and Etch Masks

Figure 2.4.4.1 outlines the procedure for generating patterned transition metal structures intended for chemical conversion. First, dilute (1:3, ma-405 to 4-methyl-2-2pentanone) negative-tone photoresist (ma-405) was spun (2000 rpm) onto a Si (100) wafer or 1/2" square quartz chip and baked at 95 °C for 4 min. The patterned PDMS master was then placed into conformal contact with the resist and exposed to broadband UV light for several seconds. After exposure, the wafer/chip was developed, oxygen plasma cleaned for 1 min at 1 Torr and placed into an e-beam evaporation chamber. Typically a thin adhesion layer (<5 nm) of Cr or Ti was deposited followed by 25-90 nm of the transition metal to be converted. The patterned metal was revealed after lift-off of the photoresist.

Figure 2.4.4.2 shows the steps used to generate dot or parallelogram etch masks using positive-tone photoresist. Positive-tone photoresist (Shipley 1805) was spin cast (5000 rpm) onto a Si (100) wafer and cured at 105 °C for 4 min. After curing, the PDMS dot mask was brought into conformal contact with the resist, exposed to UV light, and developed to reveal small (<250 nm) photoresist posts. The patterned wafer was then cleaned in oxygen plasma to remove residual photoresist left over after development. The patterned substrate was then placed in a e-beam evaporation chamber followed by deposition of 20 nm of Cr or Ti. After the

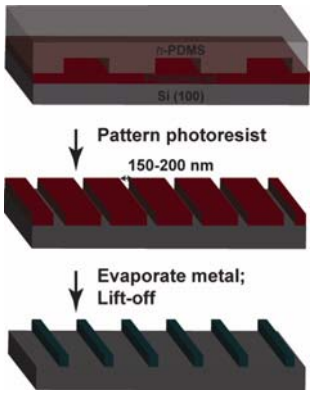

Figure 2.4.4.1. Fabrication scheme for generating metal nanopatterns.

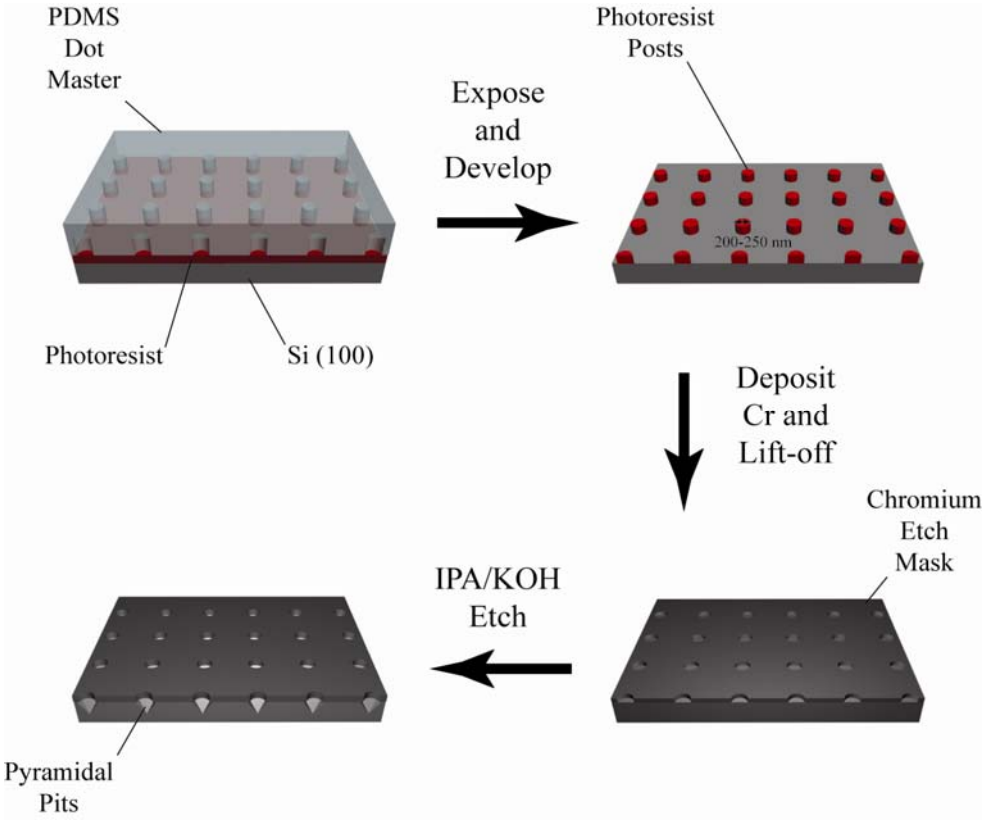

Figure 2.4.4.2. Scheme of fabrication process for generating patterned metal film etch mask.

photoresist was lifted-off using 1165 remover (MicroChem), the patterned metal film was ready to use as an anisotropic etch mask.

2.5 Summary

Several advancements in fabrication and analytical techniques have enhanced our abilities to create and characterize functional nanoscale materials. (1) We have developed a suite of techniques that combines top-down nanoscale patterning (PSP) and bottom-up methods (chemical conversion) to provide an approach for generating patterned and free-standing TMCs, and noble metal nanostructures. (2) The development of sophisticated thin film analytical techniques such as, GXRD, has enabled the structural characterization of patterned nanostructures with low pattern densities (~2 μm spacings). (3) Recent progress in optical spectroscopy has facilitated characterization of single nanostructures.

Chapter 3

Confined Crystal Growth using MoS_2 as a Model System[38]

Adapted from: Adv. Mat. **17**, 2837-2841 (2005)

3.1 Introduction

We have developed a general strategy for patterning nanoscale crystalline structures on surfaces—in particular, metal sulfide nanomaterials—by combining top– down nanoscale patterning techniques with bottom–up chemical methods. This chapter reports an approach to generate molybdenum disulfide (MoS_2) nanostructures by the sulfidation of patterned sub-300 nm features of molybdenum metal. Our method can be used to pattern arbitrary shapes of MoS_2 nanostructures with independent control over their width, height, and length. In addition, we can control the orientation of the crystals by placing the patterned substrates at different locations in the quartz tube furnace. These nanostructures can be fabricated with variable pitch, over large areas (cm^2), and on a range of insulating and conducting substrates (e.g., sapphire, fused silica, and silicon).

MoS_2 is a layered semiconducting material that has shown promise in chemical sensors,[39] in solar cells,[40] in catalysis,[41-43] and for low-friction surfaces.[44-46] Recent studies have suggested that reducing the size of the MoS_2 crystals can improve their lubrication properties in bearings, O-rings, or other heavy-wear applications.[47] The ability to pattern MoS_2 nanostructures and other metal-sulfide materials on surfaces with specific sizes and shapes has the potential to optimize and improve their usefulness. MoS_2 ribbons have successfully been grown on the step edges of highly oriented pyrolytic graphite by electrochemical methods.[48, 49] Although the heating of MoO_2 nanowires in H_2S for several days could achieve increased lateral dimensions of MoS_2 ribbons, control of other aspects of this system, such as the height, the spacing, and the overall length of the ribbons, remains a challenge.

3.2 Experimental Methods

Fabrication of Arrays of Molybdenum Nanostructures: Phase-shifting photolithography (PSP) was used to generate sub-300 nm trenches in negative-tone photoresist (Microposit ma-405) by exposing broadband UV light (365–436 nm) through *h*-PDMS (hard poly(dimethylsiloxane)) masks patterned with recessed features (lines, rings, or dots). The features in the *h*-PDMS mask were <200 nm in width (smallest was 100 nm; largest was <300 nm) and 400 nm in height. Instead of producing features at the *edges* of the mask, which is typically observed in standard PSP, the nanopatterned mask generated features in negative photoresist that were *identical* in size and pitch to the *h*-PDMS mask.[21] We then used an e-beam to deposit a thin (< 5 nm) Cr adhesion layer followed by 25–90 nm of Mo onto the patterned substrates. The photoresist was removed by agitation in acetone and 1165 developer.

Chemical Conversion of Molybdenum Nanopatterns: Silicon substrates patterned with Mo lines, rings and dots were placed in a 2" diameter (13" length) tube furnace. Oxygen was purged from the system by five consecutive cycles of pumping down to <20 Torr and refilling with 99.99% Ar gas. The temperature was slowly ramped (2 °C min–1) to 850 °C under a flow of Ar (200 standard cubic centimeter per minute (sccm), P_{Ar} <690 Torr) and H_2S gas (20 sccm, P_{H2S} <70 Torr); samples were held at this temperature for 4 h. After 4 h, the chamber was purged for 20 min. with Ar gas (1500 sccm) and allowed to cool to ambient temperature over a 90 min period.

Characterization of MoS_2 Nanostructures: Field emission scanning electron microscope (FE-SEM) images were obtained on a LEO 1525 microscope. PXRD spectra were measured

using a Rigaku D/MAX 8 X-ray diffractometer. XPS spectra were taken using an Omicron ESCA Probe X-ray photoelectron spectrometer.

3.2.1 Oxidation State Characterization of as Deposited Precursor Mo

We characterized the chemical composition of as-deposited Mo films to improve our understanding of how the nanopatterned Mo lines could be converted to MoS_2 nanostructures. Upon their removal from the e-beam evaporator, the samples were immediately exposed to oxygen (from ambient conditions). We verified the presence of MoO_x (mixture of Mo/MoO_2) in the thin film Mo lines using XPS. Figure 3.2.2 shows the XPS spectra of a Mo film after e-beam deposition and exhibits peaks indicative of mixed MoO_x. Our MoO_x peak (228.65 eV) is shifted by -1.25 eV from the reference value (229.9 eV) from MoO_2 and +0.55 eV from the reference Mo peak (228.1 eV). Oxygen vacancies and small amounts of elemental Mo in the MoO_2 lattice could be responsible for the shift toward elemental Mo.

3.2.2 Generation of Mo Patterned Structures using PSP and Chemical Conversion to MoS_2

Figure 3.2.3 outlines the procedure for patterning MoS_2 nanostructures. First, phase-shifting photolithography was used to generate sub-300 nm trenches in negative-tone photoresist and is described in greater detail in section 2.4.4.[21] We then deposited, by electron-beam (e-beam) deposition, a thin (< 5 nm) Cr adhesion layer followed by 25–90 nm of Mo onto the patterned substrates. After removal of the photoresist, we placed the Mo patterns into a quartz-tube furnace (13 in. in length, 1 in.= 2.54 cm) for chemical conversion. The temperature was slowly ramped (2 °C min–1) to 850 °C under a flow of Ar and H_2S gas; the sample was held at this

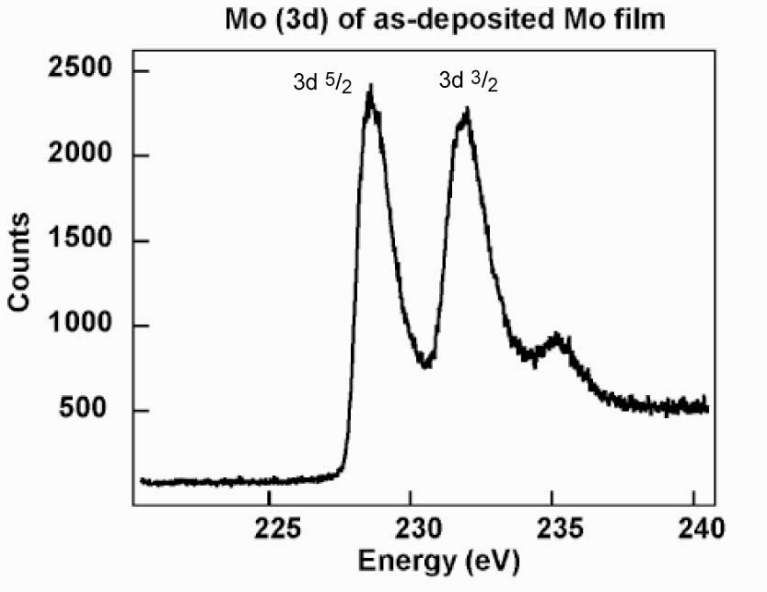

Figure 3.2.2. XPS spectra of the Mo films after e-beam deposition exhibit peaks indicative of mixed MoO_x (228.65 eV).

temperature for 4 h and allowed to cool to room temperature. These reaction conditions are similar to previous studies that used H_2S gas as the sulfur source for the conversion of MoO_2/O_3 to MoS_2. Notably, our reaction times are significantly shorter (4 h compared to 24–84 h). [48-50]

3.2.3 Structural Characterization of Patterned MoS_2 and Thin Film

FE-SEM images of patterned Mo lines 90 nm in height (90 nm Mo lines) and the MoS_2 lines obtained after sulfidation are shown in Figures 3.2.4.1A–C. The MoS_2 nanostructures in Figures 3.2.4.1B,C are morphologically distinct from each other. The former image depicts crystals that overlap and are oriented parallel to the silicon substrate, while the latter image shows crystals that are oriented perpendicular to the substrate. What is interesting is that the patterned Mo lines were subjected to identical reaction conditions (gases, temperatures) except for their *position* inside the tube furnace. Samples placed 9–10" downstream from the entrance formed MoS_2 plates parallel to the substrate (200 nm in height), while samples 3–4" downstream produced MoS_2 plates oriented nearly perpendicular to the substrate (50–150 nm thickness on the edge).

To investigate how the conversion of Mo to MoS_2 depended on the thickness of the initial Mo layer, we reacted patterns of 25 nm tall Mo lines (Figure 3.2.4.1D) with H_2S in the furnace. SEM images reveal that the preferential orientations of MoS_2 crystals formed 9–10" downstream from the entrance of the furnace (Fig. 3.2.4.1E) or 3–4" downstream (Fig. 3.2.4.1F) are similar to the MoS_2 nanoplates formed from the 90 nm Mo patterns. Although the general morphological trends are the same for 90 nm and 25 nm samples (downstream MoS_2 nanoplates are oriented parallel to the surface), there are two distinct differences in the sizes of the MoS_2 nanocrystals: i)

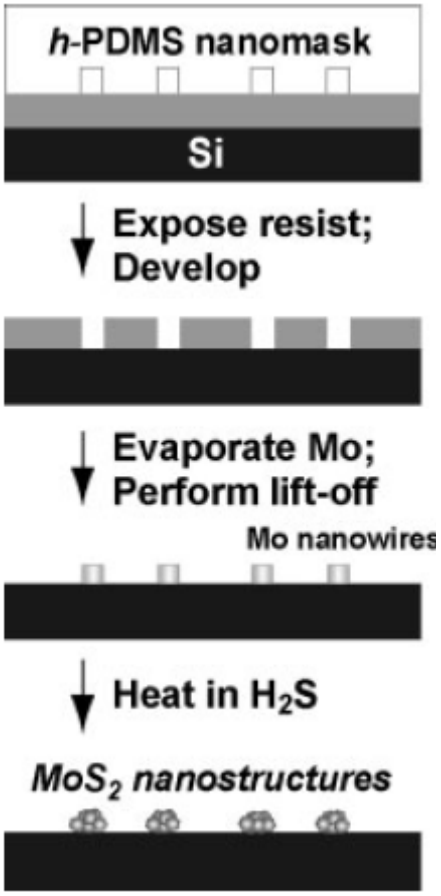

Figure 3.2.3. Schematic diagram outlining the procedure for patterning MoS_2 nanostructures; h-PDMS: hard poly(dimethylsiloxane).

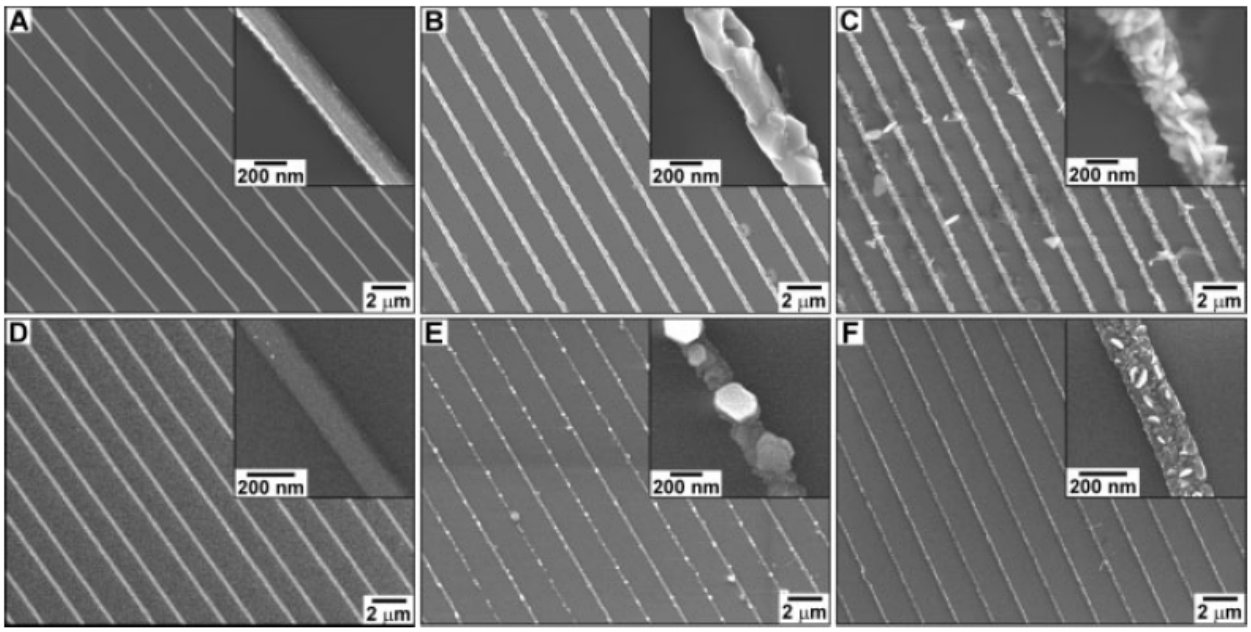

Figure 3.2.4.1. SEM images of lines of as-deposited Mo and MoS_2. A) 90 nm tall Mo lines. B) MoS_2 lines converted from (A) after reacting with H_2S gas. The nanoplates are oriented parallel to the surface and overlap with each other. C) MoS_2 lines converted from (A) with crystals oriented perpendicular to the surface. D) 25 nm tall Mo lines. E) MoS_2 lines converted from (D) placed far downstream of the tube furnace entrance. F) MoS_2 lines converted from (D) placed near the entrance of the tube furnace.

the MoS_2 crystals formed from the 25 nm Mo samples that lie parallel to the surface do not overlap significantly with neighboring crystals; and ii) the thicknesses of the crystals oriented perpendicular to the surface are reduced substantially. Measured from SEM images, the MoS_2 nanoplates parallel to the surface had widths ranging from 100 to 200 nm, and the plates perpendicular to the surface had edge thicknesses of 5–15 nm. We propose that variations in the H_2S concentration along the tube furnace or the decomposition of H_2S gas along the length of the furnace contribute to the preferential orientation of MoS_2 nanocrystals.

Two possible mechanisms can explaining sulfidation of our as-deposited Mo metal nanopatterns: i) conversion of the MoO_x present in the patterns to MoS_2 crystalline nanostructures[49] and/or ii) direct sulfidation of the Mo metal nanopatterns.[51] For both mechanisms, there is a limited range over which the reaction conditions are optimal. We found that at higher temperatures (> 900 °C) and/or longer reaction times (> 12 h), the silicon substrate and the Mo patterns degrade; at lower temperatures (< 800 °C) and/or shorter times (< 4 h) the Mo patterns were neither fully converted to MoS_2 nor highly crystalline.

One advantage of our nanopatterning followed by chemical conversion method is that nanostructures other than straight lines can be generated. Figure 3.2.4.2 demonstrates that our technique can be used to pattern individual, 300 nm diameter MoS_2 dots, as well as curved nanostructures. The MoS_2 dots highlight that crystalline structures can be formed directly from amorphous Mo/MoO_x materials. Interestingly, when the lateral size of the Mo patterns becomes larger than 300 nm, the MoS_2 nanocrystals do not exhibit the dramatic orientational preference depending on their growth position in the furnace. MoS_2 films and patterned microstructures consisted of a mixture of crystals oriented parallel and perpendicular to the substrate.

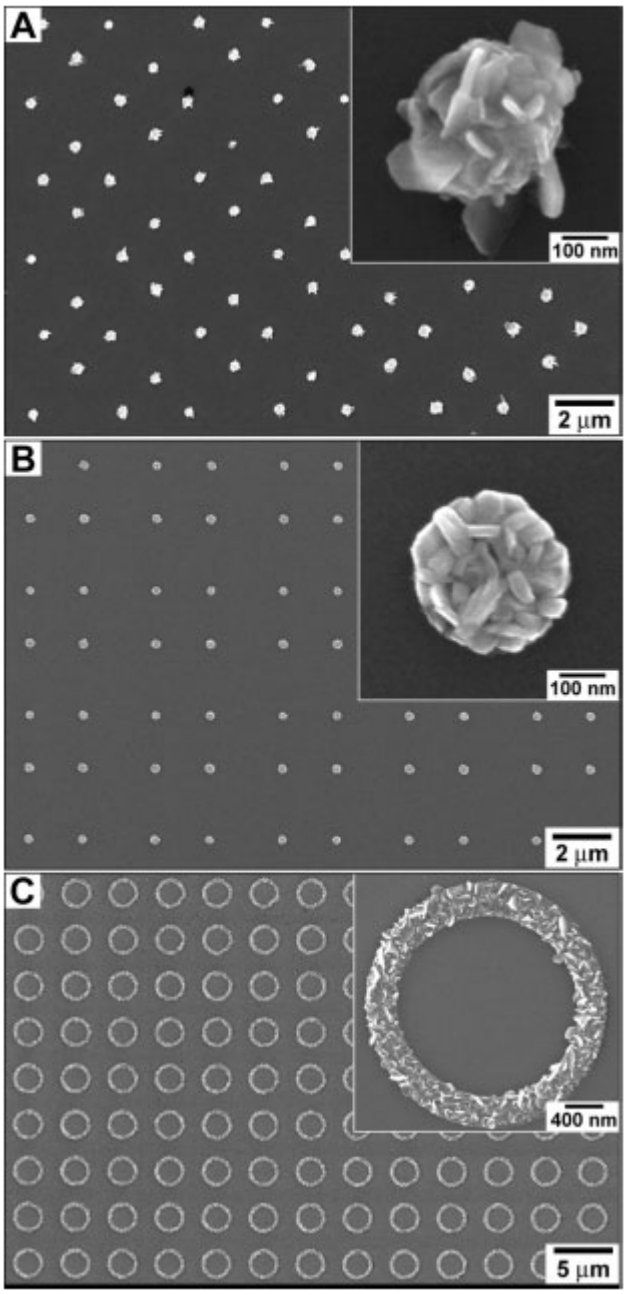

Figure 3.2.4.2. SEM images of A) MoS_2 dots converted from 90 nm tall Mo dots, and B) 25 nm tall Mo dots. C) Rings of MoS_2 nanostructures illustrate our ability to form crystals on curved patterns.

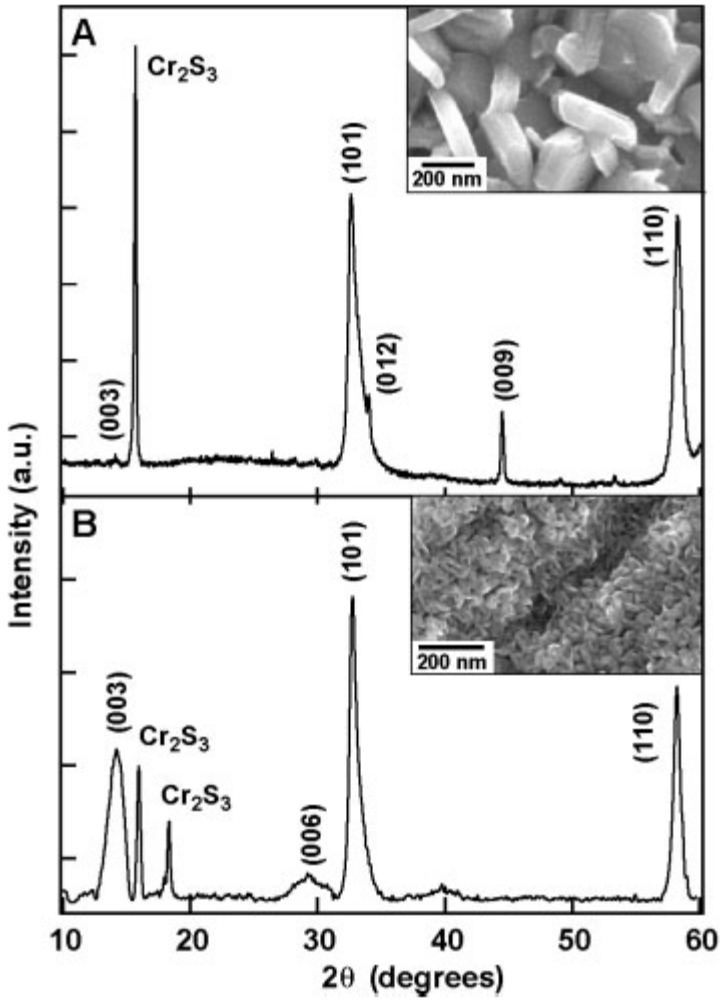

Figure 3.2.4.3. PXRD patterns of MoS_2 nanostructured films where the majority of the nanoplates were oriented A) nearly perpendicular to the substrate, and B) mostly parallel to the substrate. Insets depict portions of the MoS_2 nanostructured films. The contributions of the Cr_2S_3 under layer to the PXRD patterns are indicated, and the large intensity of the MoS_2 (009) peak in (A) most likely is from the (11–6) peak of Cr_2S_3.

Powder X-ray diffraction (PXRD) spectra of patterned MoS_2 nanostructures and MoS_2 nanostructured films are consistent with bulk 3R–MoS_2 (Powder Diffraction File, PDF#00-017-0744) comprised of Mo atoms trigonally coordinated with S atoms in a sandwich arrangement with three layers per unit cell. Because of the different orientations of the MoS_2 nanocrystals in the nanocrystalline films, certain peaks are exaggerated in the PXRD spectrum. For example, the (003) peak is very small in films when a majority of the plates are oriented normal to the surface (Figure 3.2.4.3A); MoS_2 films with a higher percentage of plates parallel to the surface exhibit the (003) peak (Figure 3.2.4.3B). Patterned MoS_2 lines possessing crystals oriented parallel to the substrate show only a weak, single (003) peak. In most of the diffraction patterns, a large peak near $2\theta = 15.9°$ is observed. It is possible that this peak is from a Cr_2S_3 layer (PDF # 03-065-4651), which forms when the underlying Cr adhesion layer reacts with the H_2S, since our reaction conditions are similar to those used to synthesize Cr_2S_3.[52]

3.2.4 Optical Characterization and Empirical Formula Determination of thin film MoS_2

We measured the optical properties of MoS_2 nanostructures on quartz substrates by UV-vis absorption spectroscopy. Figure 3.2.5.1 shows two distinct absorption maxima corresponding to the A1 and B1 exciton peaks in crystalline MoS_2.[49, 53] The position of the peaks for MoS_2 films formed by sulfidation of the 25 nm Mo and 90 nm Mo films were nearly identical (within 5 nm). To further verify the empirical formula of our metal chalcogenide thin film after sulfidation at 850 °C for 4 h we examined the oxidation states of Mo and looked for the presence of S using XPS. Figure 3.2.5.2 shows detailed spectra of the Mo and S regions of interest. The Mo $3d^{5/2}$ at 229.1 eV indicates the presence of Mo in the 4^+ oxidation state yielding MoS_2 as our primary product. In the spectra we noticed that the Mo $3d^{3/2}$ at 232.5 eV exhibits greater than expected

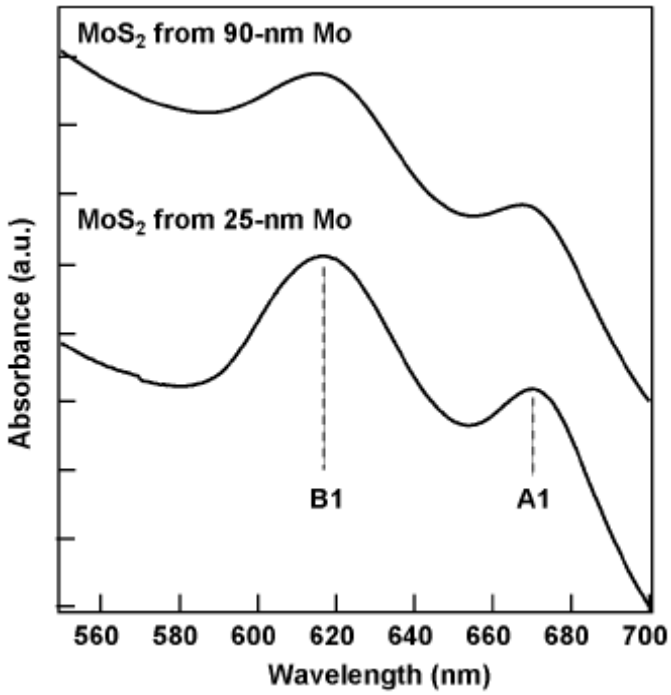

Figure 3.2.5.1. UV-vis absorption spectroscopy of MoS_2 nanostructured films converted from Mo films that were 90 and 25 nm thick. The positions of the two exciton peaks, A1 and B1, are indicated by dashed lines.

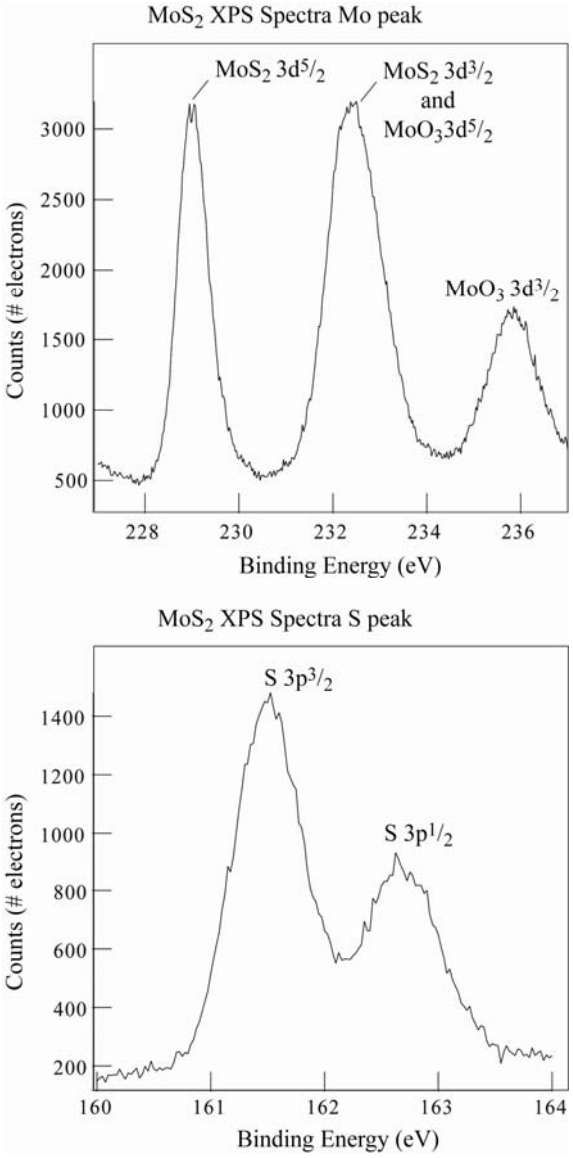

Figure 3.2.5.2 XPS spectra of the Mo and S peaks for a MoS_2 film.

intensity, plus we see an additional peak at 335.9 eV. We hypothesize that Mo $3d^{3/2}$ peak from MoS_2 is overlapping with the Mo $3d^{5/2}$ peak from the 6^+ oxidation state Mo of MoO_3 and the peak at 335.9 eV is from Mo $3d^{3/2}$ of MoO_3, which would account for the discrepancies in peak intensities and positions. Indications of MoO_3 present in the thin film sample were not evident in the GXRD spectra and we assume they are not crystalline in nature. Examination of the S spectrum indicated the characteristic S peak position at 161.5 eV further confirms the presence of a metal sulfide.[33]

3.3 Conclusions

In summary, we have demonstrated how soft-lithographic techniques can be used to generate patterns of MoS_2 nanostructures with controllable orientation, height, width, and shape. Limitations of our strategy include: i) supporting surfaces for the nanostructures need to be stable at high temperatures (850 °C), and ii) toxicity of the sulfur source. Since most technologically relevant surfaces (e.g., Si, SiO_2, and GaAs) can withstand such temperatures, this drawback is minimized. Also, careful gas-handling and proper exhaust equipment can alleviate concerns about H_2S. These patterning methods, moreover, offer a general approach to create patterned metal oxide and chalcogenide nanostructures on surfaces, which can be integrated directly into device platforms. Our ability to control the orientation of the MoS_2 nanocrystals may also be important in applications such as catalysis and sensors, which become more effective with the increased surface area of materials.

Chapter 4

Chemical Nanofabrication[54]

Adapted from J. Mater. Chem. **17**, 1866-1869 (2007)

4.1 Introduction

Transition metal chalcogenide (TMC) materials are important in a range of applications from solar cells[55] to low friction surfaces[46] to battery electrode materials.[56] The ability to generate nanoscale structures of TMC materials offers new opportunities to optimize and improve their properties and to extend their usefulness. For example, fullerene-like TMCs (e.g. WS_2, MoS_2 and TiS_2) intercalated with Li exhibit greater loading capacity and are less air sensitive compared to bulk crystals; such properties are important for battery storage capacity.[57] WS_2 nanotubes exhibit a red shift in their band gap as the diameter of the tube decreases because of the increased elastic strain imposed on the molecular sheets,[57] and their high aspect ratios have made them useful as tips for scanning probe microscopies.[58] WS_2 and MoS_2 nanostructures have also demonstrated potential as additives to conventional lubricants by improving their general wear characteristics.[59]

Similar to synthetic approaches, chemical nanofabrication—the combination of nanoscale patterning and chemical methods[60]—can also create new types of functional nanostructures with unexpected properties. Nanoscale solid state ionic conducting materials, such as Ag_2S, have been used as a basis for quantized controlled switching and have achieved faster switching speeds as a function of size.[61] Ribbons (5–50 mm wide) of Si and GaAs with thicknesses between 20–300 nm can be repeatedly stretched and compressed with no loss of structural or electronic integrity and have potential for use in flexible electronics.[62, 63] Nanoscale wells with zL volumes in silicon substrates have functioned as nanoscale beakers to grow crystalline CdS nanoparticles at room temperature.[20] Single crystalline nanowires of Ag_2Se and CdSe have also been synthesized by a low temperature chemical transformation of pre-formed Se nanowires.[64] In addition, we have

found that a reduction in the size of Mo metal nanopatterns prior to their chemical conversion in H_2S gas resulted in the preferential orientation of MoS_2 nanocrystals within patterned MoS2 structures.[38]

4.2 Experimental Methods

Fabrication of Arrays of Nickel and Silver Nanostructures: Phase-shifting photolithography (PSP) was used to generate sub-200 nm trenches in negative-tone photoresist (Microposit ma-405) by in a similar manner as list in for Mo. We then used an e-beam to deposit a thin layer of Ti (~2 nm) 70 nm of Ni or 60 nm Ag onto the patterned substrates. The photoresist was removed by agitation in 1165 developer.

Fabrication of Free-standing NiS_2 Mesostructures: PSP was used to generate sub-200 nm raised parallelograms in positive tone photoresist (Shipley 1805) by exposing broadband UV light (365-436 nm) through *h*-PDMS mask patterned with recessed features (parallelograms). The features in the *h*-PDMS mask were 2 μm across the parallel sides, ~2.5 μm across the long points and ~1.5 μm across the short points and 400 nm in height. As with standard PSP, features are created at the edges of the structures creating an outline of a parallelogram with the dimensions of the inlayed features. I used an e-beam to deposit a thin layer (20 nm) of Cr to use as an etch mask. The photoresist was removed by agitation in 1165 developer, followed by anisotropic etching the exposed underlying Si (100) substrate using aqueous KOH/IPA solution yielding trenches in the Si substrate. The trenches are V shaped because they are stabilized along the Si (111) plane. E-beam evaporation was used to deposit 70 nm of Ni into the trenches, followed by removal of the Cr etch mask and excess Ni. The microscale Ni parallelograms were

chemically converted in the same manner of other Ni patterned arrays listed below. After chemical conversion the structures were released from the Si (100) template by etching away Si substrate until the structures were released from the etched trenches.

Chemical Conversion of Nickel Nanopatterns: Silicon substrates patterned with Ni lines, rings, parallelograms and dots were placed in a 1" diameter (12" length) tube furnace. Oxygen was purged from the system by five consecutive cycles of pumping down to <20 Torr and refilling with 99.99% Ar gas. The temperature was slowly ramped (2 °C min^{-1}) to 400 °C under a flow of Ar (85 sccm, P_{Ar} <646 Torr) and H_2S gas (15 sccm, P_{H2S} <119 Torr); samples were held at this temperature for 12 h. After 12 h, the chamber was purged for 20 min. with Ar gas (1000 sccm) and allowed to cool to ambient temperature over a 90 min period.

Chemical Conversion of Silver Patterns: Silicon substrates patterned with Ni lines, rings, parallelograms and dots were placed in a 1" diameter (12" length) tube furnace. Oxygen was purged from the system by five consecutive cycles of pumping down to <20 Torr and refilling with 99.99% Ar gas. For chemical conversion to Ag_2S the temperature was slowly ramped (2 °C min^{-1}) to 100 °C under a flow of Ar (85 sccm, P_{Ar} <646 Torr) and H_2S gas (15 sccm, P_{H2S} <119 Torr); samples were held at this temperature for 20 min. After 20 min, the chamber was purged for 20 min. with Ar (1000 sccm) and allowed to cool to ambient temperature over a 90 min period. For conversion of Ag to Ag_2Se the chamber was purged several times with Ar and evacuated to ~8 mTorr and held at 200 ºC for 20 min in the presence of sublimed Se vapor. The chamber was then purged with Ar and allowed to cool to room temperature.

Fabrication of Heterogeneous Crossed Arrays of NiS_2 and Ag_2Se Lines: PSP photolithography was used to pattern Ni line following the procedure listed for fabrication of Ni

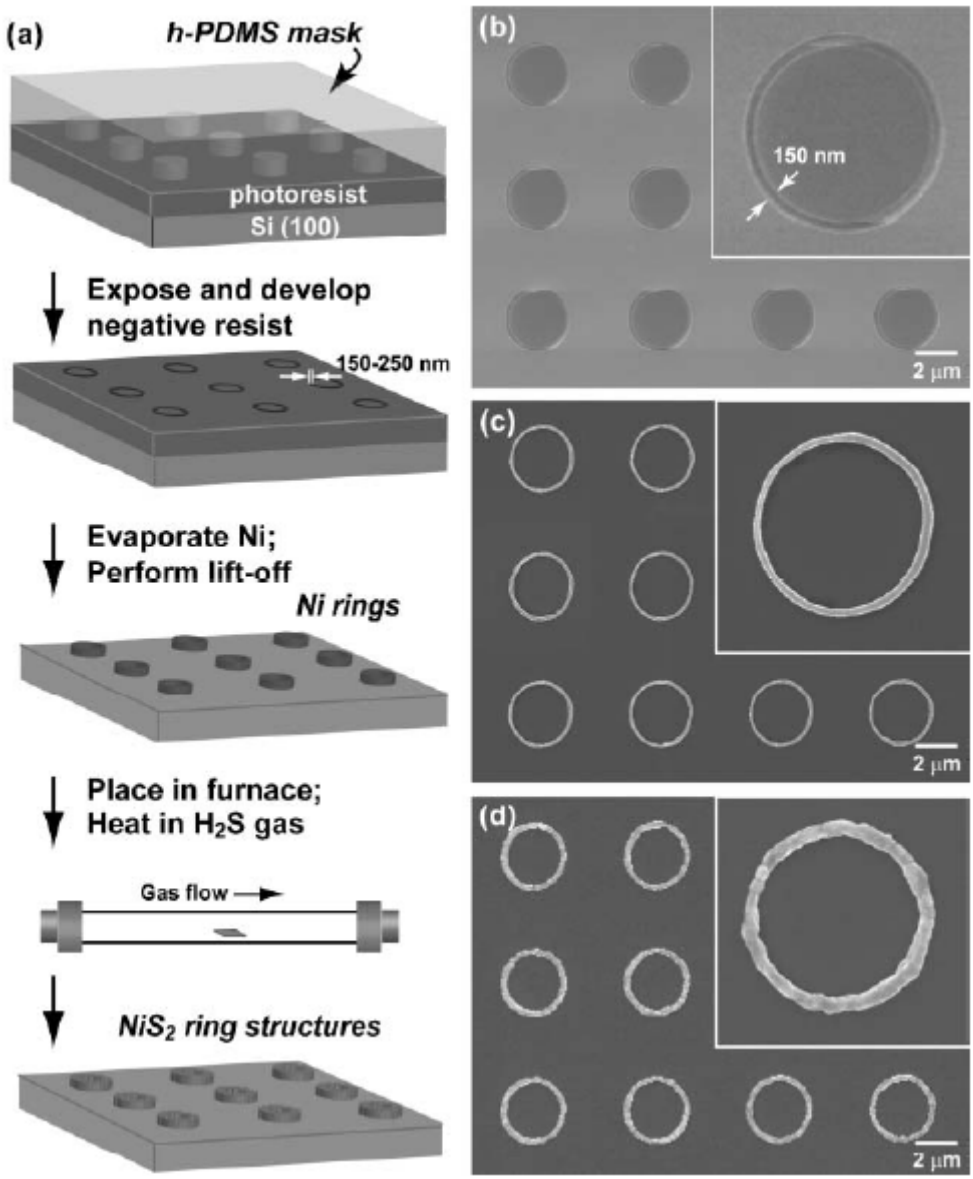

Figure 4.2.2. (a) Schematic outline of the procedure to generate arrays of TMCs. (b) Scanning electron microscopy (SEM) image of an array of recessed rings in negative-tone photoresist. (c) SEM image of an array of Ni rings. (d) SEM image of an array of NiS_2 rings after chemical conversion of Ni rings in (b). All insets are 4 μm x 4 μm.

nanostructures. The arrays of Ni lines were chemically converted following the procedure listed for Ni nanopatterns. Ag line arrays were added to the already patterned NiS_2 structure using the procedure listed for patterning arrays of Ag nanostructures. Chemical conversion of the Ag line arrays to Ag_2Se was performed using the methods in the chemical conversion of Ag patterns.

4.2.1 Fabrication of Ni Patterned Structures and Chemical Conversion to NiS_2

Figure 4.2.2A outlines our procedure to pattern TMC structures composed of nanoscale crystals. We have illustrated this general approach by focusing on a specific metal, nickel, patterned on a Si substrate. First, phase shifting photolithography (PSP) with a *h*-PDMS mask patterned with recessed 3 μm circles was used to generate rings with sub-200 nm trenches in a negative-tone photoresist (ma N-405) (Figure 4.2.2B).[65] We then deposited by e-beam evaporation a thin (~2 nm) adhesion layer of Ti followed by 70 nm of Ni to produce Ni rings after lift-off of the photoresist (Figure 4.2.2C). To convert the metal to its metal sulfide, we placed the nanopatterned Ni sample into a 1 in quartz tube furnace for 10 h at 400 ºC (2 uC min21) under a flow of argon (P_{Ar} ~646 Torr) and H_2S (P_{H2S} ~114 Torr) gases. The Ni rings were converted to NiS_2 ring structures, whose widths were 260–290 nm and heights were 115–140 nm (Figure 4.2.2D).

A variety of nickel chalcogenides (NiS, Ni_3S_2 and NiS_2) are generally stable at room temperature using similar synthetic conditions as our studies. Further analysis using XPS was performed to confirm the empirical formula the structural data suggests. Figure 4.2.3 shows the spectra for the 400 nm spaced NiS_2 lines. The inset indicates an electron binding energy of

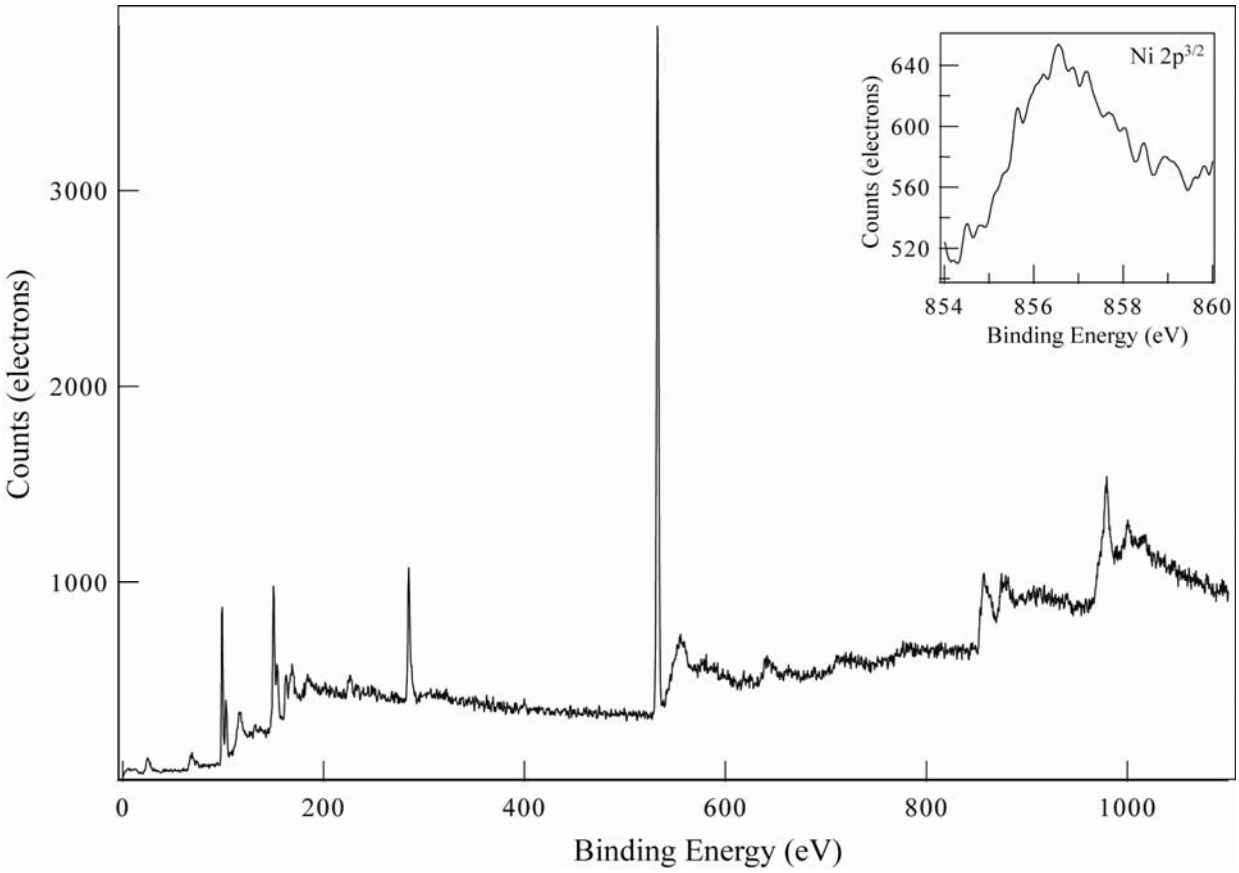

Figure 4.2.3. XPS spectra of patterned 400 nm spaced NiS_2 lines. Inset shows characteristic Ni^{4+} peak of NiS_2.

856.55 eV for Ni $2p^{3/2}$ peak and indicates an empirical formula of NiS_2 further confirming our structural X-ray data.

4.2.2 Structural Characterization of Patterned NiS_2

Surprisingly, the NiS_2 structures were composed of nanocrystals that overlapped with each other to form a continuous network (Figure 4.2.4). The edges of the crystals followed the direction of the patterned metal structures, both for curved (Figure 4.2.4A, insets) and straight patterns (Figure 4.2.4B). Figure 4.2.4B shows one dimensional arrays of NiS_2 lines that are spaced by 400 nm. Although the crystals in these lines were also connected, on careful inspection, it was obvious that individual lines were not identical; the crystal facets had slightly different orientations along the patterned lines. To determine the crystal structure of the patterned NiS_2 materials, we used GXRD. This technique allowed us to characterize the crystal structure of relatively low density nanostructures, and at the same time, preserve their integrity on a surface. GXRD spectra were consistent with bulk cubic NiS_2 (PDF #01-089-3058, SG:Pa3) (Figure 4.2.4C). In some cases, the X-ray angle of incidence was not steep enough, and we occasionally picked up peaks from the underlying Si substrate.

In contrast to our previous work on MoS_2 nanostructures,[38] the crystals in the NiS_2 structures did not exhibit preferential orientation depending on their location within the tube furnace. It is possible that this difference is because of the different crystal structures, since synthetic MoS_2 is a layered material with Mo atoms trigonally coordinated to S atoms in a sandwich arrangement with three layers per unit, while NiS_2 is cubic with Ni atoms coordinated

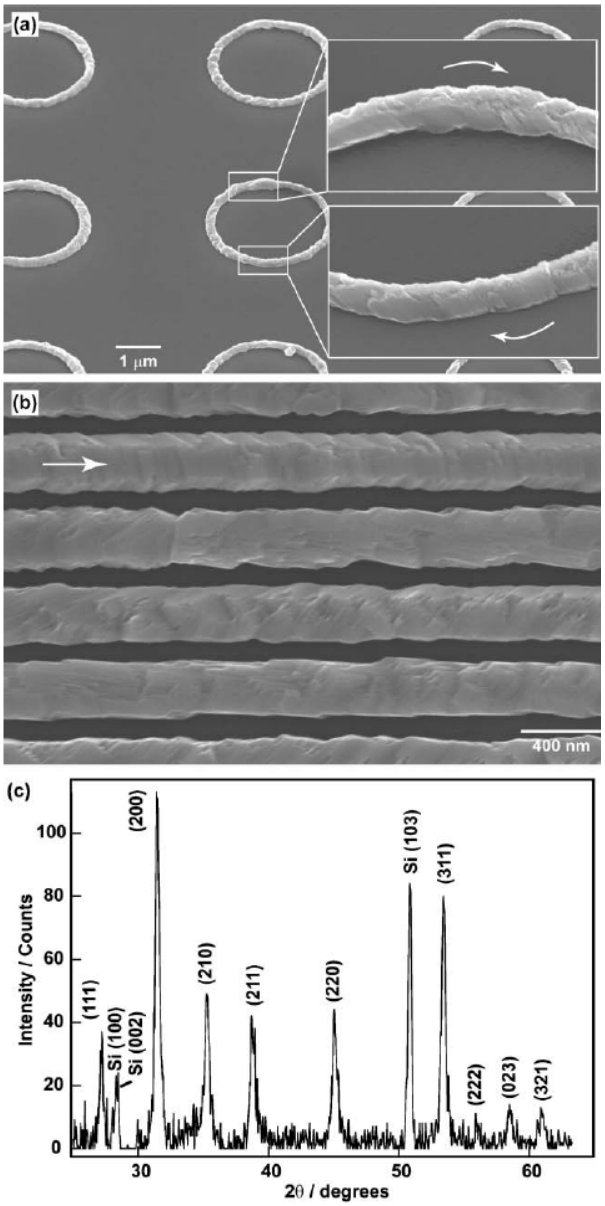

Figure 4.2.4. (a) SEM image of arrays of NiS_2 rings. The tilt angle is 45°. The insets depict how the nanocrystals within the NiS_2 ring overlap with each other and follow the curved direction of the pattern. (b) SEM image of NiS_2 lines generated on a 400 nm pitch. Each line is a continuous structure although the nanocrystal facets are oriented at slightly different angles along the line. (c) GXRD spectrum of nanopatterned NiS_2 lines exhibiting characteristic peaks for cubic NiS_2 (PDF #01-089-3058).

to six S atoms in a pyrite lattice structure. Also, the crystals comprising the MoS_2 structures were more discrete, while for NiS_2, the overlapping nanocrystals formed continuous structures.

4.2.3 Fabrication and Structural Characterization of Patterned Ag_2Se

Our chemical nanofabrication approach to TMC nanomaterials can be readily extended to form metal selenide nanostructures. Instead of reaction of the patterned metal nanostructures in the tube furnace with H_2S gas, we can expose them to Se vapor formed by sublimation of solid Se powder. This quasi-solid state reaction with solid Se has been used by others to synthesize one dimensional nanostructures.[66] After carrying out PSP with *h*-PDMS masks patterned with 2 μm lines spaced by 2 μm on negative photoresist, we deposited 60 nm of Ag and performed liftoff to generate lines of Ag. We then placed this substrate into the tube furnace with Se powder. The chamber was purged several times with argon gas and evacuated to ~8 mTorr and held at 200 ºC for 20 min. Figure 4.2.5A depicts lines of Ag_2Se that were formed after reacting the Ag lines with Se. Noticeably, the structures do not exhibit well-formed facets like the NiS_2 structures. The GXRD spectrum revealed, however, that the Ag_2Se structures were orthorhombic (PDF #01-089-2591, space group P2221) (Figure 4.2.5B).

4.2.4 Fabrication and Elemental Analysis of Patterned NiS_2/Ag_2Se Heterogeneous Arrays

Because we use soft masks for photolithography, we can perform multiple patterning steps to create arrays of structures of different TMC materials on the same substrate. We have developed a two-stage conversion process to fabricate crossed arrays of different materials. This procedure can be summarized by four steps: (1) nanopatterning the first metal (M1) using PSP

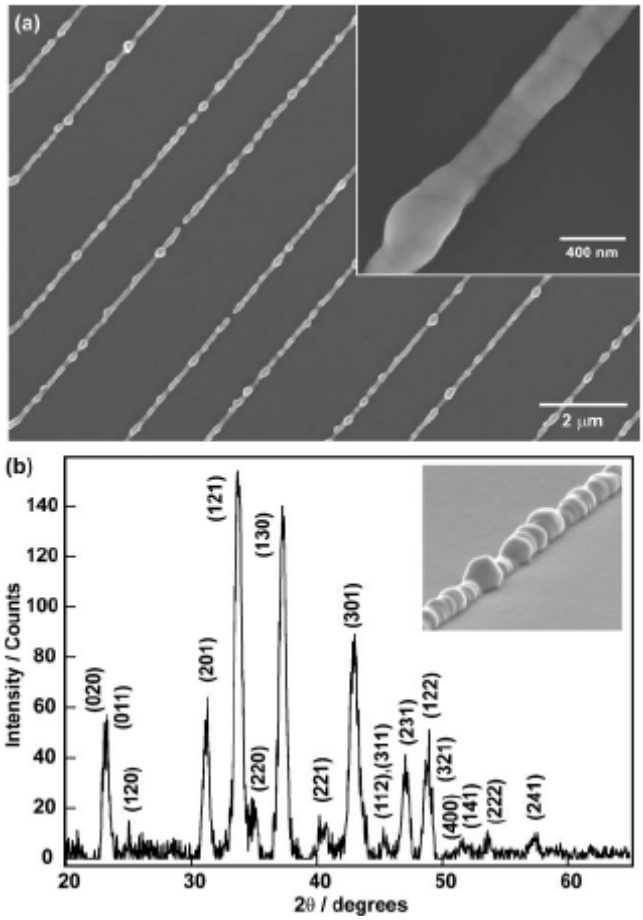

Figure 4.2.5. (a) SEM image of Ag lines converted to Ag_2Se using quasi-solid state reaction conditions. Inset shows a zoom-in of one of the Ag_2Se lines. (b) GXRD spectrum of lines in (a) exhibiting characteristic peaks for orthorhombic Ag_2Se (PDF #01-089-2591).

followed by deposition and lift-off; (2) converting M1 to its sulfide analog; (3) nanopatterning the second metal (M2) using PSP followed by deposition and lift-off; and (4) converting M2 to its selenide counterpart.

We have carried out this procedure by first generating 250 nm lines of NiS_2 on a 2 μm pitch. Then, we spin-cast negative-tone photoresist (ma N-405) over the NiS_2 pattern and performed PSP with masks patterned with microscale lines having variable pitch and oriented perpendicular to the NiS_2 lines. Even after evaporation of 60 nm of Ag followed by lift-off of the photoresist, the NiS_2 structures were robust and stayed intact, which provides additional evidence that the structures were continuous. This secondary patterning could not be achieved using standard Cr masks in contact photolithography because the hard contact would damage the substrates. We then placed the NiS_2/Ag crossed arrays into a quartz tube furnace along with Se powder source material and evacuated and heated the chamber to 200 ºC. Figure 4.2.6 shows arrays of lines of NiS_2 crossed by lines of Ag_2Se, which appear to be continuous across the intersection. The lines in the array can also be on any pitch because they are determined by the PDMS mask. We have demonstrated this versatility by patterning the Ag_2Se lines on a 2 μm (Figure 4.2.6A) and 10 μm (Figure 4.2.6B) pitch. EDX analysis indicated that each line was composed of the intended elements and that very little Se was incorporated into the NiS_2 structures under these conditions.

4.2.5 Generation of Free-standing NiS_2 Structures

Because the NiS_2 nanomaterials are continuous, it should be possible to release them from the surface to form free-standing TMC structures. For this case, we modified our

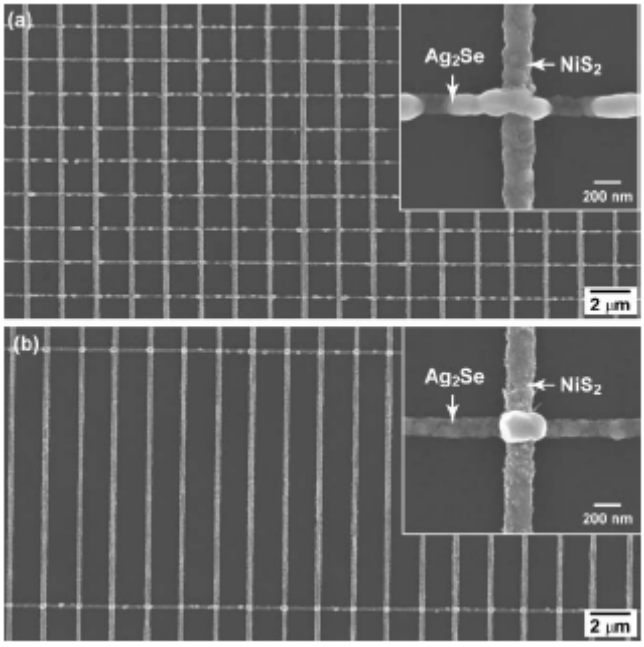

Figure 4.2.6. (a) SEM image of lines of NiS_2 crossed by lines of Ag_2Se generated in a two-step process as described in the text. The Ag_2Se lines are spaced by 2 μm. The inset shows that the Ag_2Se lines remain continuous over the underlying NiS_2 lines. (b) SEM image of lines of NiS_2 crossed by lines of Ag_2Se where the Ag_2Se lines are on 10 μm pitch.

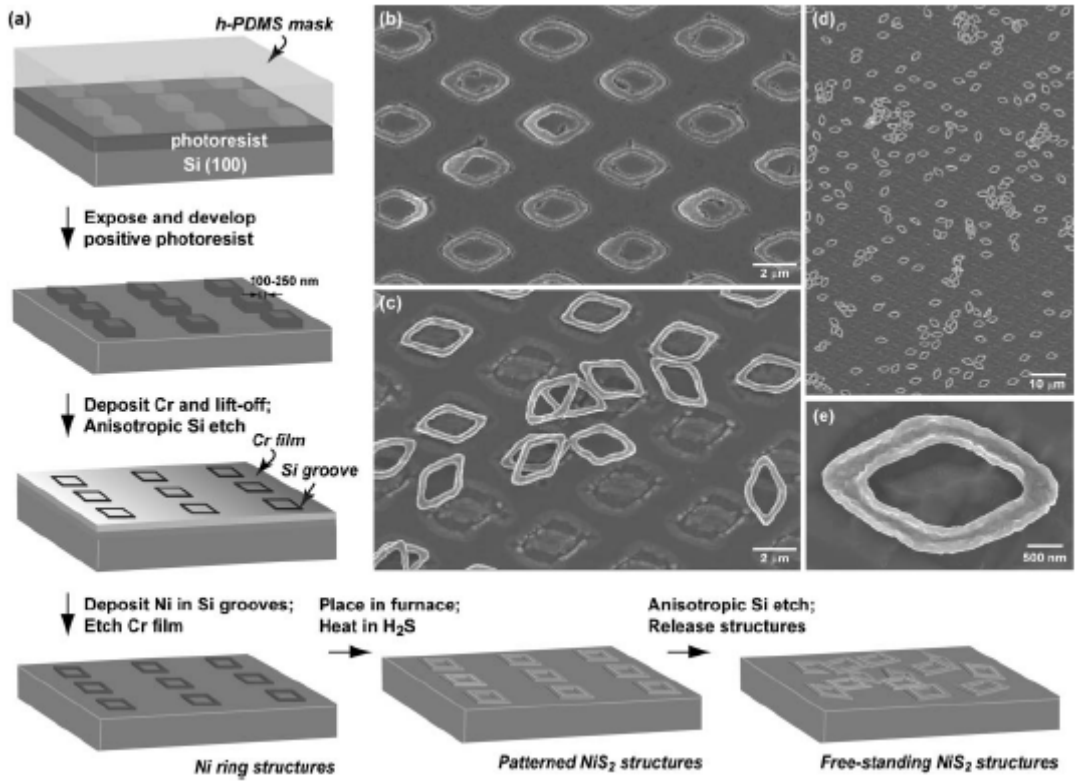

Figure 4.2.7. (a) Schematic outline of the procedure to generate free-standing NiS_2 structures. (b) SEM image of NiS_2 parallelograms within etched Si grooves. (c) SEM image of free-standing NiS_2 structures after they have been released from the substrate by a brief anisotropic Si etch. (d) Large-area image of freestanding NiS_2 parallelograms. (e) Zoom-in of an individual NiS_2 structure, which is robust and intact after removal from the template.

nanopatterning method but kept the chemical conversion conditions the same. Figure 4.2.7A outlines the procedure for creating free-standing NiS_2 nanostructures. First, we performed PSP using *h*-PDMS masks patterned with recessed parallelograms on positive-tone photoresist (Shipley 1805) to produce outlines of the parallelograms supported on Si (100) substrates.[21] We then deposited a thin (30 nm) layer of Cr and performed lift-off to form a Cr film with slots exposing the underlying Si. The sample was placed in an anisotropic Si etch (isopropanol–KOH, 72 ºC), where the exposed Si was etched to form recessed ‘‘V’’ grooves, whose facets were Si (111) planes. We then deposited 50 nm of Ni into the grooves and removed the Cr film by wet chemical etching to form Ni rings inside the Si grooves. These Ni ring patterns were then placed into the tube furnace and converted to NiS_2 (Figure 4.2.7B). These NiS_2 structures supported by Si were subjected briefly (50–80 s) to an anisotropic Si etch to release the parallelograms (Figure 4.2.7C–E). The free-standing structures can also be dispersed in solution or transferred to other substrates.

4.3 Conclusions

In summary, we have demonstrated how chemical nanofabrication provides a general method to produce patterned and freestanding TMC nanomaterials. We have used this bottom-up meets top-down strategy to generate arrays of continuous NiS_2 and Ag_2Se structures with controlled shapes and sizes, crossed line arrays of NiS_2/Ag_2Se, and free-standing NiS_2 structures. These types of TMC nanostructures cannot easily be obtained by other chemical or fabrication-only methods. A limitation of our strategy for crossed arrays is that the metal sulfide nanopatterns must be stable in a Se-rich atmosphere (and at elevated temperature); any such

reactivity could be useful, however, to create patterned solid solutions. Also, one drawback of our technique to generate freestanding structures is that the TMC should be compatible with KOH etch solutions; however, a dry Si etch in XeF_2 can also release the TMC nanostructures. Our ability to generate nanopatterned arrays of different TMCs, and in addition, freestanding TMC nanostructures, will certainly open new scientific prospects and contribute to emerging technologies based on TMCs.

Chapter 5

Solid-state Chemistry of TaS_2 Nanostructures

Adapted from: J. Solid State Chem. **181**, 1621-1627 (2008)

5.1 Introduction

Metal chalcogenide materials are important in a broad range of applications from solar cells[67, 68] to catalysts[42, 69] to low-friction surfaces.[46, 70] In particular, transition metal chalcogenides (TMCs) have demonstrated promise for battery electrode materials,[56, 71] photovoltaic devices,[40] and photocatalysts.[43, 72] Reducing the size and controlling the shape of TMCs to nanoscale dimensions has resulted in enhanced properties compared to bulk. For example, fullerene-like TMC nanotubes (e.g. MoS_2, TiS_2, and WS_2) are more air-stable and show a greater loading capacity of Li.[73] Both characteristics are important for battery storage capacity.[57] In addition, HfS_2 nanotubes show photoluminescence that is blue-shifted compared to the bulk.[74] Spherical inorganic fullerene TMC materials, such as WS_2, also demonstrate superior wear resistance and longer lubrication lifetimes compared to TMC powders.[47, 57] Hollow MoS_2-nanoparticles can exhibit an order of magnitude lower frictional coefficient than bulk sputtered MoS_2 and are more stable because of their closed cage configuration.[75]

Other layered TMC materials, such as TaS_2, $TaSe_2$, and $NbSe_2$, show complex electronic properties such as superconductivity and charge density wave (CDW) behavior.[76-79] In the case of $NbSe_2$, the superconducting transition temperature (T_c) can be reduced by decreasing the number of layers.[80] $NbSe_2$ nanostructures consisting of ca. 12 layers have shown a slight decrease (0.3 K) in T_c.[81] Conversely, TaS_2 nanowires have exhibited an elevated T_c compared to the bulk (0.6–3.4 K).[82] Confining the size or reducing the dimension of the materials has also facilitated investigations of new mesoscopic phenomena. For example, one-dimensional (1D) chains of TaS_3, $NbSe_3$ and $TaSe_3$ have been especially important in studying CDW behavior in reduced dimensions.[83-85] Nanowires and ribbons made from $NbSe_3$ demonstrate an order of

magnitude suppression in the resistivity around the CDW transition temperature compared to bulk $NbSe_3$ from size effects, and wires consisting of less than 2000 chains show insulating behavior at low temperatures (<50 K).[66, 86] Also, in 1D TaS_3 nanostructures, CDWs were responsible for ohmic conduction at low temperatures.[87] Despite the intriguing possibilities of observing quantum-size effects on superconductivity, there are few reports on different synthetic methods to nanoscale diselenide materials.[76, 79, 81, 85, 88-90]

Using broad classifications, there are three different routes to generate nanoscale TMC materials: (1) chimie douce (soft chemical) synthesis, (2) solvothermal methods, and (3) hightemperature solid-state reactions. MoS_2 nanoclusters have been synthesized within inverse micelles[r], and MoS_2, $MoSe_2$, WS_2 and WSe_2 nanoparticles have been grown starting from transition metal (M) carbonyl and chalcogen (E) precursors.[91] Nanoparticles produced using solution-based methods, however, are generally amorphous and require further annealing treatments to improve crystallinity. Although solvothermal methods can produce improved crystalline materials compared to chimie douce processes, a challenge is size control.[92-95] An advantage is that a variety of binary (e.g. $NiSe_2$, $CoSe_2$) and ternary metal chalcogenides (e.g. Ag_8SnS_6, and Ag_8SnSe_6) can easily be grown using solvothermal chemistry.[96-99] Under high-temperature conditions, inorganic fullerene-like nanoparticles and multiwalled inorganic nanotubes have been produced, such as WS_2 nanotubes starting fromWO_{3-x} particles[58] and MoS_2, WS_2, and $MoSe_2$ particles and nanotubes from the decomposition of ammonia salts ($(NH_4)_2ME_4$) or metal trichalcogenides (ME_3).[100-104] None of these methods, however, can facilitate the assembly of nanoscale TMC materials into specific locations on a substrate. Such control is critical for investigation of their properties at the single nanostructure level and also for direct

integration into devices. Early efforts for organizing MoS_2 nanowires have used the step edges of a graphite surface as a template,[48, 49] although the structures are usually transferred to a different substrate for chemical sensing and other applications.

5.2 Experimental Methods

Fabrication of Arrays of Tantalum Nanostructures: Phase-shifting photolithography (PSP) was used to generate sub-200 nm trenches in negative-tone photoresist (Microposit ma-405) by in a similar manner as list in for Mo. We then used an e-beam to deposit a thin layer of Ti (~2 nm) 50 nm of Ta onto the photoresist patterned fused silica substrates. The photoresist was removed by oxygen plasma followed by sonication in DI water.

Chemical Conversion of Tantalum Nanopatterns: Fused silica substrates patterned with Ta lines were placed in a 1" diameter (12" length) tube furnace. The patterned Ta was oxidized under atmospheric gas conditions at 650-850 ºC for 10 h. After confirmation of Ta oxide formation the substrates where placed back into the tube furnace and oxygen was purged from the system by five consecutive cycles of pumping down to <20 Torr and refilling with 99.99% Ar gas. The temperature was slowly ramped (2 °C min^{-1}) to 950 °C under a flow of H_2S gas (15 sccm) and ~3 Torr pressure; samples were held at this temperature for 12 h. After 12 h, the chamber was purged for 20 min. with Ar gas (1000 sccm) and allowed to cool to ambient temperature over a 90 min period.

Anodization of Ta_2O_5 nanotube: Ta sheets were placed in a solution consisting of 50 ml of H_2SO_4 and 3 ml HF (49%) with a Pt counter electrode. The Ta sheet was anodized at 30 V for 10 minutes. The sheet was then rinsed with DI water into a beaker and yielded 80 nm diameter

~13 μm long tubes of Ta_2O_5. The tubes were vacuum filtered and rinsed 10 times with 18 MΩ water to ensure removal of acids.[105]

Conversion of Ta_2O_5 to TaS_2: The tubes were ground with a mortar and pestle for ~5 min to separate the tubes and then placed into a 1" quartz tube furnace. Oxygen was purged from the system by five consecutive cycles of pumping down to <20 Torr and refilling with 99.99% Ar gas. The temperature was slowly ramped (2 ºC min^{-1}) to 650 ºC under a flow of H_2S gas (15 sccm) and ~3 Torr pressure; samples were held at temperature for 1-48 h. After, 1-48 h, the chamber was purged for 20 min with Ar gas (1000 sccm) and allowed to cool to ambient temperature.

5.2.1 Fabrication of Patterned Ta Lines on Fused Silica

Although we have highlighted the advantages of this chemical conversion approach to generate TMC nanomaterials, there are two potential limitations: (1) the metal deposited by e-beam must not damage the photoresist template and (2) the substrate supporting the metal nanopatterns must not react with the chalcogen source. The former is problematic primarily for refractory metals (such as Ta, Nb, and Mo), which can cause significant heating of the e-beam chamber during deposition. The elevated temperatures cause the photoresist polymer to crosslink, and standard lift-off in organic solvents cannot be easily used to produce the metal nanopatterns. We overcame this challenge by first exposing the photoresist to oxygen plasma and then sonicating the substrate in water. Ta nanopatterns were fabricated using this modified approach to lift-off.

5.2.2 Investigation and Analysis of Temperature Effects on the Crystal Structure of Ta_2O_5

In contrast to the Mo system, which could be converted directly to MoS_2 from the as-deposited Mo nanopatterns, the Ta patterns did not converted to TaS_2 without an intermediate oxidation step. Not surprisingly, we found that the oxidation temperature (650–850 ºC) had a significant impact on the crystallinity and morphology of the tantalum oxide (Figure 5.2.3). As the temperature increased from 650 to 750 ºC, the characteristic peaks of orthorhombic Ta_2O_5 (Pmm2, PDF #00-025-0922) increased in intensity while the FWHM decreased. Such changes are characteristic of improved crystallinity, although no marked differences in morphology were observed in SEM images (Figure 5.2.3, insets). Under an increased oxidation temperature of 850 ºC, the Ta2O5 lines were faceted and adopted an alternate orthorhombic structure (Ibam, PDF#00-054-0514). The lateral dimensions increased from ~225 to ~280 nm.

5.2.3 Chemical Conversion of Ta_2O_5 Annealed Nanowires to TaS_2 Nanowires

Figure 5.2.4 shows crystalline TaS_2 structures obtained after heating polycrystalline Ta_2O_5 (650 ºC) in H_2S at ~3 Torr at 950 ºC for 12 h. We observed that using the oxides generated at lower temperatures yielded more continuous TaS_2 nanopatterns than those from more crystalline Ta_2O_5 materials (850 ºC). Similar to 2H-MoS_2, 2H-TaS_2 is a layered material with Ta atoms sandwiched between two layers of trigonally coordinated S atoms. It is noteworthy that the TaS_2 lines were oriented near perfectly with the c-axis perpendicular to the fused silica substrate. The intense and narrow (002) peak along with the weak (101) and (104) peaks in the GXRD spectra (P63/mmc, PDF#01-080-0685) verified the crystal orientation

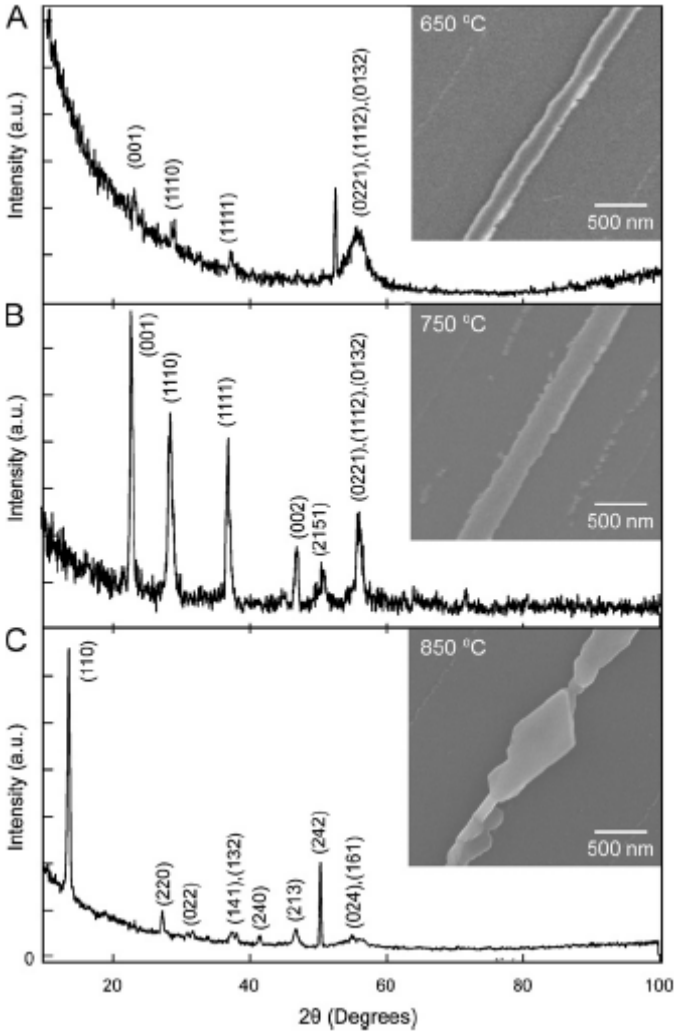

Figure 5.2.3. GAXD spectra and SEM images of lines of (A) nearly amorphous Ta_2O_5 oxidized at 650 °C, (B) crystalline Ta_2O_5 oxidized at 750 °C, and (C) Ta_2O_5 oxidized at 850 °C. Note that (B) and (C) exhibit different crystal structures.

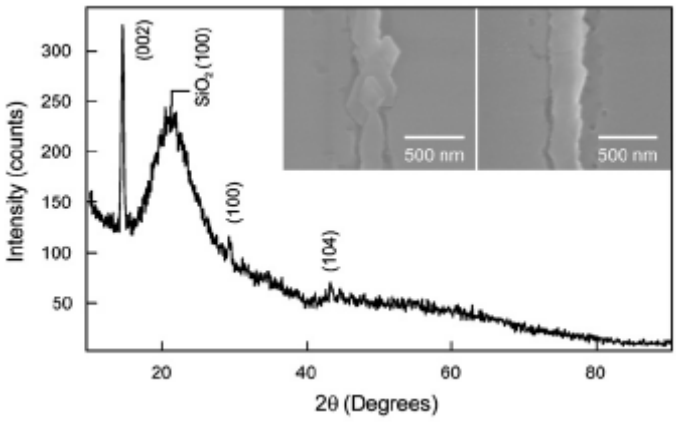

Figure 5.2.4. GAXD spectra and SEM images (insets) of near perfectly oriented TaS_2 lines with the c-axis perpendicular to the substrate.

relative to the substrate. We attribute the broad peak at ~22º to the polycrystalline silica substrate (the (100) peak is at 22.4º, PDF#01-070-3315). Some etching of the fused silica was also observed under the TaS_2 nanostructures after the reaction.

5.2.4 Chemical Conversion of Ta_2O_5 Nanotubes to TaS_2 Fullerene-like Nanotubes

To understand the conversion dynamics of the TaS_2 nanotubes the progression of sulfidation at various reaction times (1-48 h). Figure 5.2.5.1 shows the GXRD spectra of the different reaction time intervals (1, 4, 12, 24, 48h) with the inset showing typical TaS_2 nanotubes reacted for 12 h. No apparent change was noted in SEM images of different reaction time intervals. It was determined that at shorter reaction (<12 h) times large amounts of crystalline Ta_2O_5 remains unconverted and correspond to orthorhombic Ta_2O_5 (PDF#00-025-0922, SG: Pmm2). At longer reaction times (>12 h) the relative intensities in the Ta_2O_5 peaks decreases through 48 h and appears to be a diffusion limited process, although there is some crystalline Ta_2O_5 remains in the X-ray samples. Examination of the FWHM for the Ta_2O_5 peaks in the 48 h reaction time yields an average crystal size under 10 nm. The nanotubes X-ray spectra correspond to 2H-TaS_2 (PDF#01-071-3686, SG: P63/mmc).

We examined the empirical formulas of the time trial nanotubes (Figure 5.2.5.2) using XPS. Interestingly, GXRD did not indicate any structural formations other than the increasing crystallinity of TaS_2 and decreasing amounts of Ta_2O_5, XPS spectra indicate the emergence of two distinct oxidation states of Ta. The characteristic Ta peaks ($4f^{7/2}$ and $4f^{5/2}$) in TaS_2 and Ta_2O_5 overlap generating the observed spectra at 1 and 4 h, where the characteristic $4f^{7/2}$ peak occurs at ~26.6 eV. At reaction times 12 hours or longer the emergence of lower

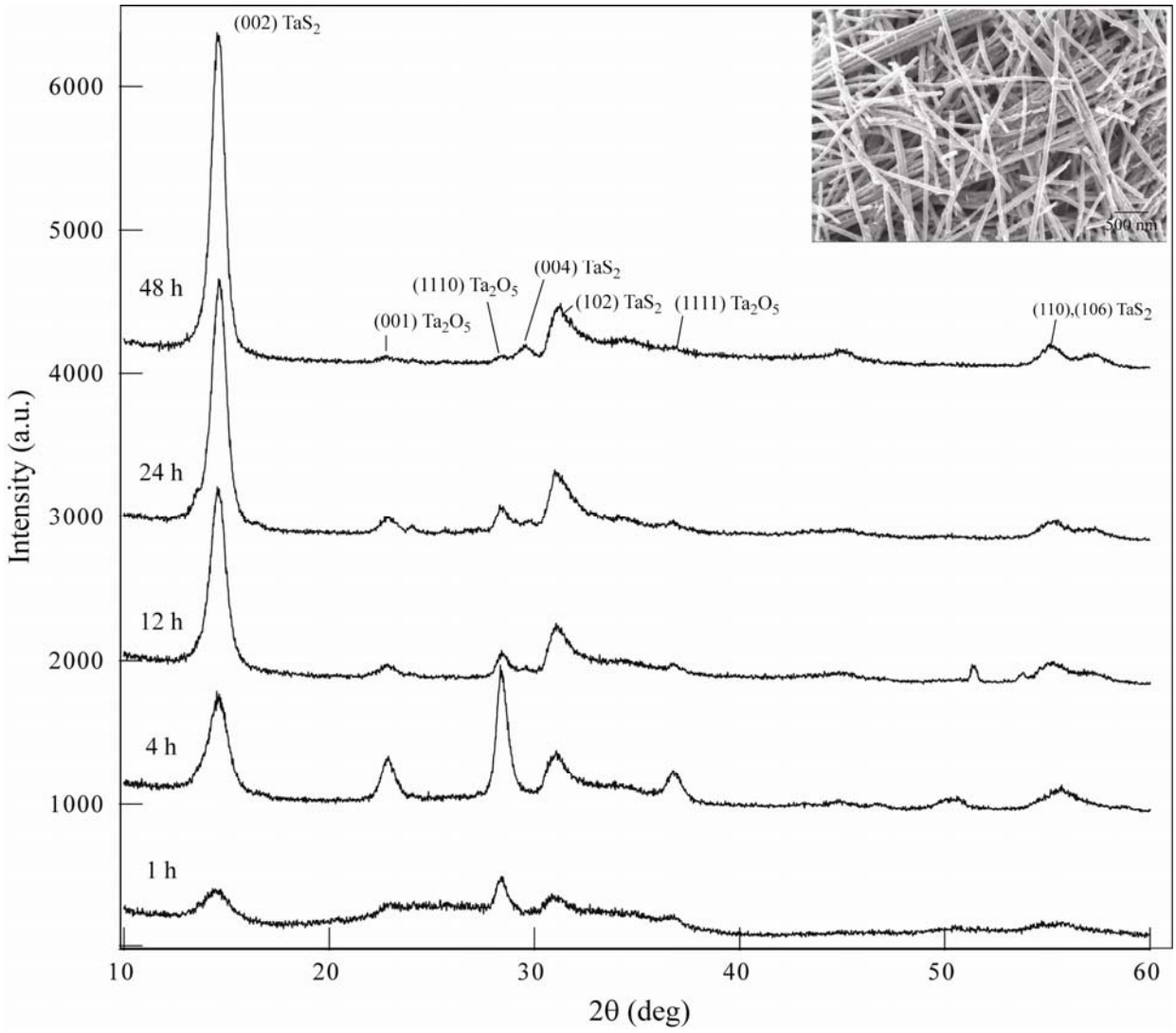

Figure 5.2.5.1. GXRD spectra of TaS_2 nanotubes converted at different time intervals 1, 4, 12, 24, and 48 h. Inset shows an SEM image of 80 nm diameter TaS_2 nanotubes.

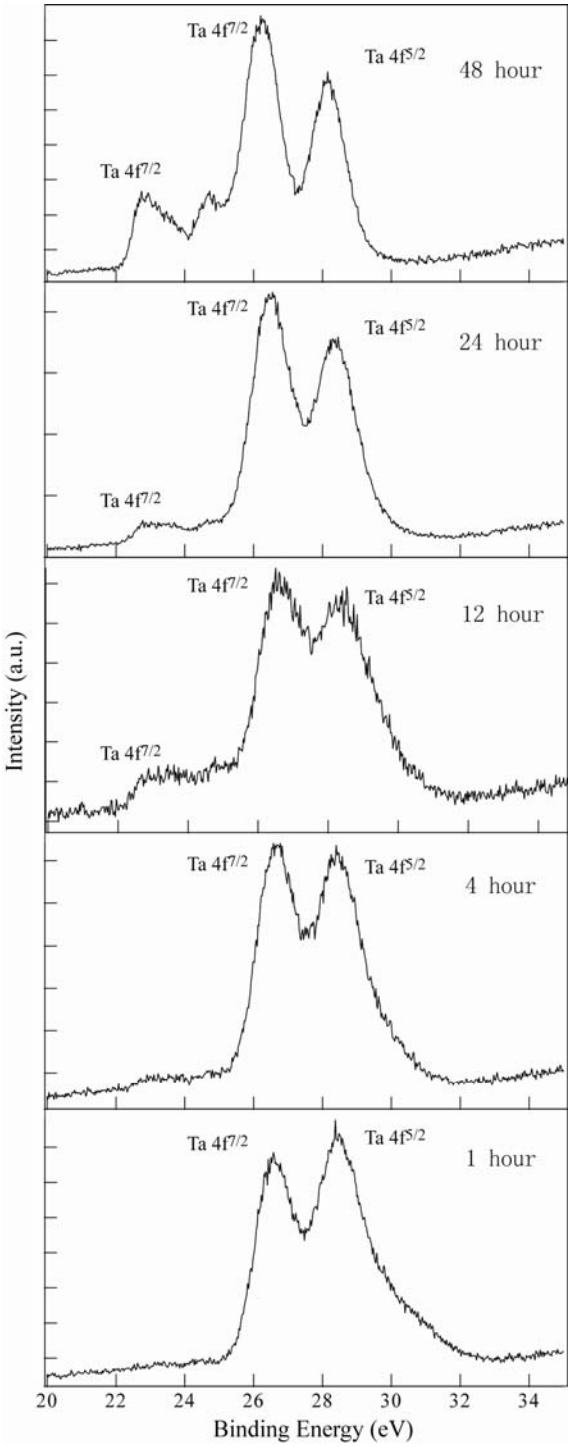

Figure 5.2.5.2. XPS spectra of TaS_2 nanotubes converted at different time intervals 1, 4, 12, 24, and 48 h.

oxidation state Ta is apparent with the appearance of an additional $4f^{7/2}$ at ~23.0 eV. We hypothesize this is because either the formation of amorphous unsaturated TaO_x or the incomplete sulfidation of Ta_2O_5 to TaS_y.

In contrast to the surface-patterned, chemical transformation method to TaS_2 nanomaterials (Figure 5.2.4), the conversion of Ta_2O_5 nanotubes did not exhibit well-faceted edges. Both the reactions, however, produced the same hexagonal crystal structure (P63/mmc), although the temperatures required to produce the TaS_2 nanomaterials were different. In the nanotube's approach, inorganic fullerene-like nanotubes were grown at 650 °C from Ta_2O_5 precursor, although no conversion was observed from the nanopatterned Ta_2O_5 structures until 950 °C.

5.3 Conclusion

TMC nanomaterials can be generated on surfaces and through conversion of anodized oxide nanotubes with control over their size, shape, and crystal structure. Such flexibility offered by chemical nanofabrication and conversion of oxide methods opens new possibilities to study finite-size effects, especially as a function of well-controlled sizes, on correlated electron phenomena in TaS_2 and $NbSe_2$. Moreover, TMC materials patterned over multiple length scales can enhance applications where large surface areas are important, such as in chemical sensing and catalysis. Because multiple, different TMC nanomaterials can now be easily patterned on a single substrate, opportunities for multiplexed sensing and broadband absorption for photovoltaics can also be envisioned. Moreover, we anticipate that these new types of patterned

and crystalline nanomaterials will enable unique prospects for interrogating solid solutions and solid-state chemical reactions at the nanoscale.

Chapter 6

Optical Properties of Tipless Pyramids

6.1 Introduction

Noble metal nanostructures exhibit strong shape and size dependant surface plasmon resonances. Because of their easily tunable properties, they have found use in a broad range of applications such as, optics[106, 107], photothermal cancer treatments,[108, 109] biological diagnostics[110] and catalysis.[111]

A wide variety of sizes and shapes of noble metal nanostructures have been generated by either: (*i*) solution based synthesis or (*ii*) template based fabrication. Solution-based synthesis uses surfactants or metal ions such as silver [112] that can stabilize specific crystal faces selectively to generate nanorods,[113, 114] prisms,[115] and tetrahedra, and many other shapes.[114-116]

Our approach uses template-based nanofabrication to control the structure of the nanopyramids systematically such that we can manipulate shape, size and thickness individually. Fabrication can also achieve high monodispersity depending on the perfection of the template because a substrate and mask layer determines the nanoparticle shape and size. Other approaches, such as nanosphere lithography, use particle-based masks where the interstitial spaces between spheres determines the size of the resulting triangles and prisms.[117, 118] Spherical particle based shadow masks have also been used to generate nanocresents by depositing metal onto polystyrene spheres followed by releasing the structures.[119, 120]

The anisotropic pyramidal shape of our nanoparticles offers a platform for understanding how specific structural features affect the multipolar plasmon resonances. Theory has predicted that there are several ways to tune the multipolar resonances of the gold pyramids (thickness, truncation, and size). We have previously shown that decreasing the height of the tipless pyramid should cause a red shift of the quadrupole peak.[121] Here we examine the effects that

progressively truncating the tip has on the optical properties. This chapter examines a modification to our PEEL[30] method where we have demonstrated an approach to generate tipless (TL) nanopyramids with variable degrees of tip truncation. We have determined that progressive tip truncation results in a linear blue-shifting of all visible plasmonic resonances. Previously we discovered that our anisotropic pyramidal particles have orientation-dependent spectra and multipolar plasmon resonances.[121]

6.2 Experimental Methods and Discussion

Fabrication of Tipless Pyramidal Mesostructures: PSP was used to generate sub-250 nm posts in positive tone photoresist (Shipley 1805) by exposing broadband UV light (365-436 nm) through *h*-PDMS mask patterned with recessed posts. Unlike standard PSP, features are an exact copy of the structures in the *h*-PDMS (<250 nm posts). I used an e-beam to deposit a thin layer (20 nm) of Cr or Ti to use as an etch mask. The photoresist was removed by agitation in 1165 developer, followed by anisotropic etching the exposed underlying Si (100) substrate using aqueous KOH/IPA solution yielding trenches in the Si substrate. The etched pits are pyramidal shaped because they are stabilized along the Si (111) plane. The template was place on a tilting rotational stage (TRS) and attached to an e-beam deposition system. The TRS was set at various angles (θ=30-55°) and spun at ~800 rpm while depositing 80 nm Au. The deposition of 80 nm of Au results in a tipless pyramid (TL) thickness of ~60 nm. After deposition the Cr etch mask and Au hole film are removed using Cr etch (Transene). The TLs were solublized by isotropically etching the Si template with XeF_2 (6 cycles of 100 s, 3 Torr XeF_2 and 10 Torr N_2) and sonicated in water.

Single Particle Scanning Spectroscopy on Mesoscale TLs: The TL was drop cast onto prepared ITO coated glass slides with numerically enumerated grids and dried with N_2. Suitable TLs are located and imaged using a SEM (LEO 1525). The sample was placed on an inverted microscope and illuminated with light from a halogen tungsten bulb through a dark field (DF) condenser with a 100X variable oil immersion condenser lens situated below it. Specifics of the instrumentation setup are list in Chapter 2. A video camera with was used to correlate the location of the particle from the SEM image to its projection on the VIS CCD detector.

6.2.1 Fabrication of Tipless Pyramids

Figure 6.2.2.1 depicts the variation of our PEEL method to generate TL structures, where the e-beam deposition step now occurs on a tilted rotating stage instead of line of sight e-beam deposition.[107] Figure 6.2.2.1A shows a scheme of the custom-built stage that enables rotational depositions at any angle between 0-90° and extends the flexibility of our fabrication process. The rotational stage is placed directly above the evaporation source material to ensure even deposition on the template, and deposited a thickness (t=60 nm) of Au where the substrate was fixed at an angles (θ) ranging from 30-55° and spun at ~800 rpm, to produce TL structures. The inset shows how the Cr etch mask is used as a shadow deposition mask to enable the generation of TL particles. Figure 6.2.2.1B indicates the representative particle heights at θ=30, 35, 45, 50, 55º. The change in height with the increasing deposition angle can be explained by considering the geometry of the shadow deposition mask. As expected, changing the θ generates larger top openings with a roughly linear relation. Isotropic XeF_2 etching and sonication were used to release the TL from the etched Si template. Figure 6.2.2.1C shows the TLs after deposition of

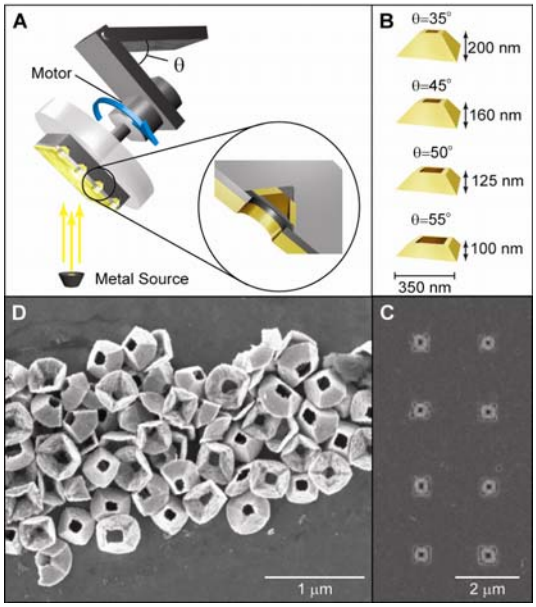

Figure 6.2.2.1. A) Diagram of TRS, B) representation of fine architectural control, C) harvested TL deposited at θ=45°, D) pyramids in template before harvesting.

Au at 45º and removal of the Cr etch/deposition mask but before they are released from the surface. We found by depositing at lower angles we can also make tipped pyramids (WT) but with square bases. Figure 6.2.2.1D shows the uniformity achieved in TLs generated at θ=45º, which is directly related to the uniformity of the shadow mask. The TLs were then released from the substrate and deposited on ITO coated glass.

Our fabrication methods also grant us a high degree of size control. Since nanostructures optical properties are dependent on size this adds another level of flexibility to our process. Figure 6.2.2.2 demonstrates the flexibility and size control by showing several TLs where the size of the photoresist post for the particles on the top of the column are smaller than the posts used at the bottom of the column, all images are 850 nm sq. All depositions for column A, B and C were held constant at 45, 50 and 55°, respectively. Figure 6.2.2.3 summarizes theoretical expectations based on a 500 nm etched pit with varying hole sizes and deposition angles.

6.2.2 Optical Characterization and Refractive Index Studies of Tipless Pyramids

To understand how shape affects optical properties, we investigate spectra for individual particles with dark field scattering microscope coupled to a UV-Vis spectrometer.[122] In our optical studies we maintained a base size of 350 nm while varying the deposition angle (θ). Maintaining the same base size was important because a nanoparticles plasmonic features exhibit size dependent properties.[35]

Figure 6.2.3.1 shows dark field scattering spectra obtained from individual TLs on ITO (n=1.80) coated glass slides with varying amounts of truncation, where the surrounding index of refraction (n) is 1.65 in order match the RI of the ITO coated glass as closely as possible. As

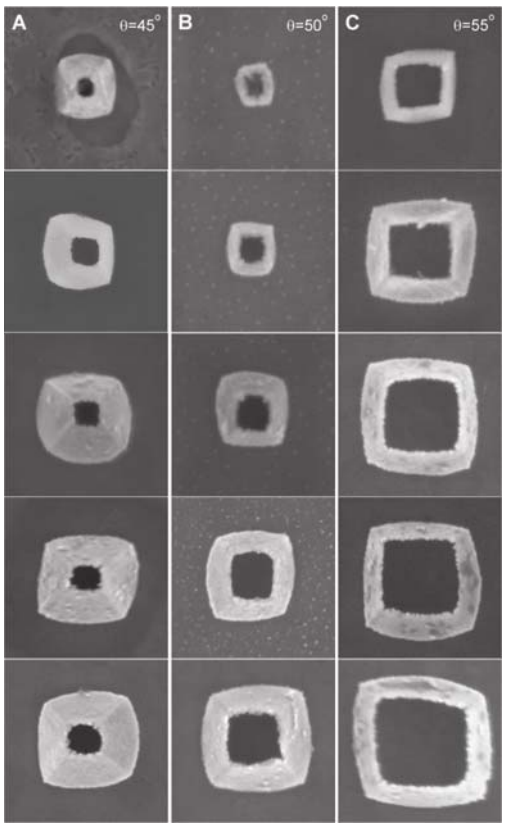

Figure 6.2.2.2. SEM images of TL deposited at θ=45° (A), 50° (B),and 55° (C) with progressively larger shadow mask hole sizes. Images are 850 nm x 850 nm.

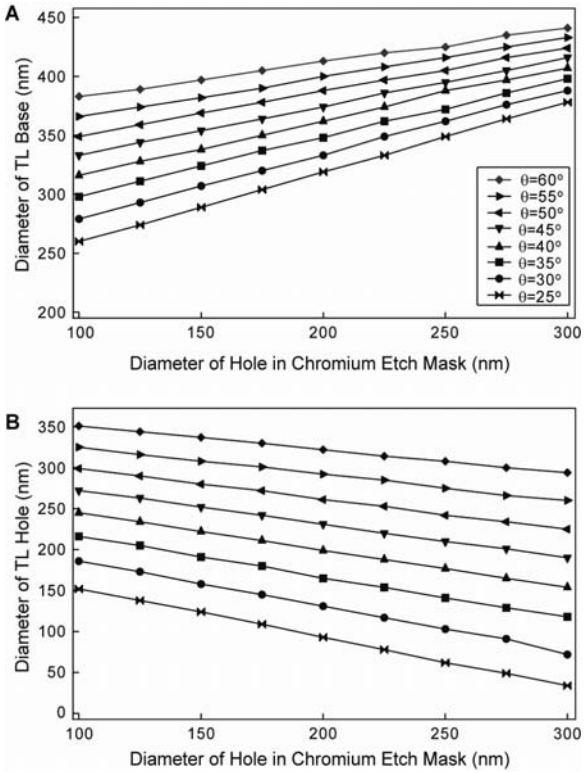

Figure 6.2.2.3. Theoretical architectural changes based on 500 nm etched pit with varying shadow mask hole sizes.

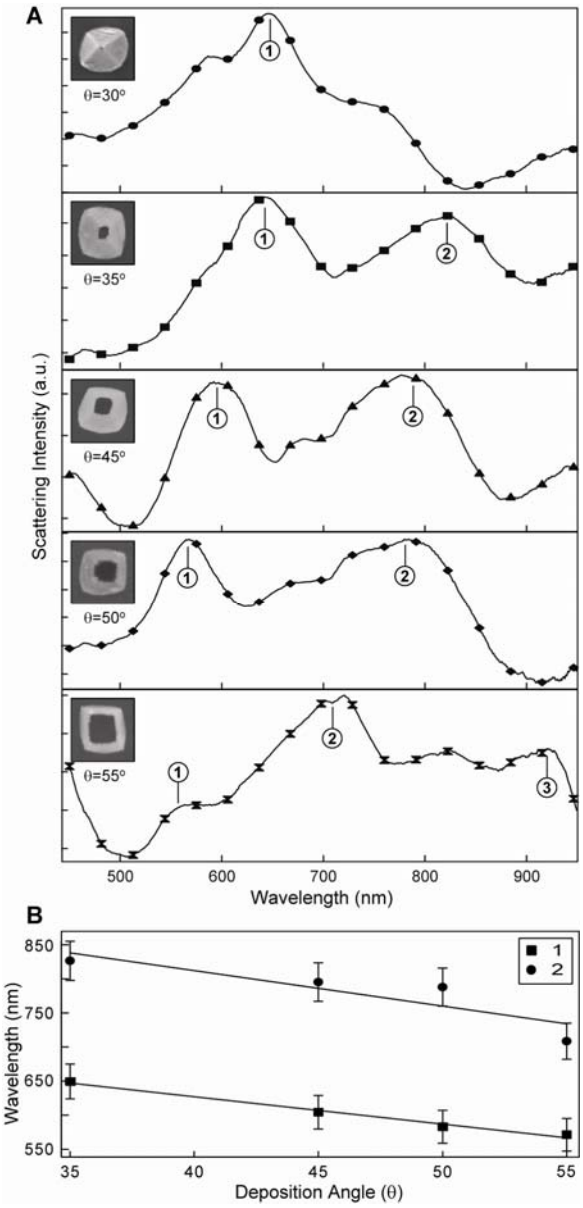

Figure 6.2.3.1. A) Scattering spectra for TL with major resonances labeled and SEM images. B) Optical trends observed for resonant features.

seen in the insets of figure 6.2.3.1, low deposition angles (θ≤30°) result in square based pyramids with tips, while higher angles (θ≥30°) generate TL with progressively more ring like structures. In our studies all pyramids thicknesses were 60 nm. The 350 nm square based WT (θ=30º) exhibited spectra with three resonances (~585, 650, and 760 nm). Interestingly, the square based WT exhibit sharper resonances than we observed in our previous work with circular based WT, where a broad convoluted resonance ~600 nm was observed.[36, 121] Additionally, the 650 nm resonance labeled as peak 1 appears in all square based pyramid spectra. Further, the resonance labeled as peak 2 only appears in TL and may be an interaction between the upper and base square rings. Figure 6.2.3.1B tracks the trends of both observable peaks labeled (1 and 2) of the TLs as they shift to bluer wavelengths as the deposition angle (and the hole size) increases with peaks 1 and 2 shift from 650 nm to 570 nm and 830 nm to 710 nm. The shift to bluer wavelengths can be understood by considering that as we truncate the pyramids we are effectively decreasing the surface area, volume and sharp edges for the surface plasmon interactions to occur, thus confining the plasmons to smaller areas and higher energies.

To determine how the resonances of TLs change under different dielectric environments (*n*), we surrounded the particles with oils of different *n* (Figure 6.2.3.3, 6.2.3.4). Such wavelength shifts can also be used to determine the refractive index sensitivity, which often compressed to a single value called a figure of merit (FOM).[123] The FOM is determined by the following:

$$FOM = \frac{\Delta\lambda / \Delta n}{FWHM}$$

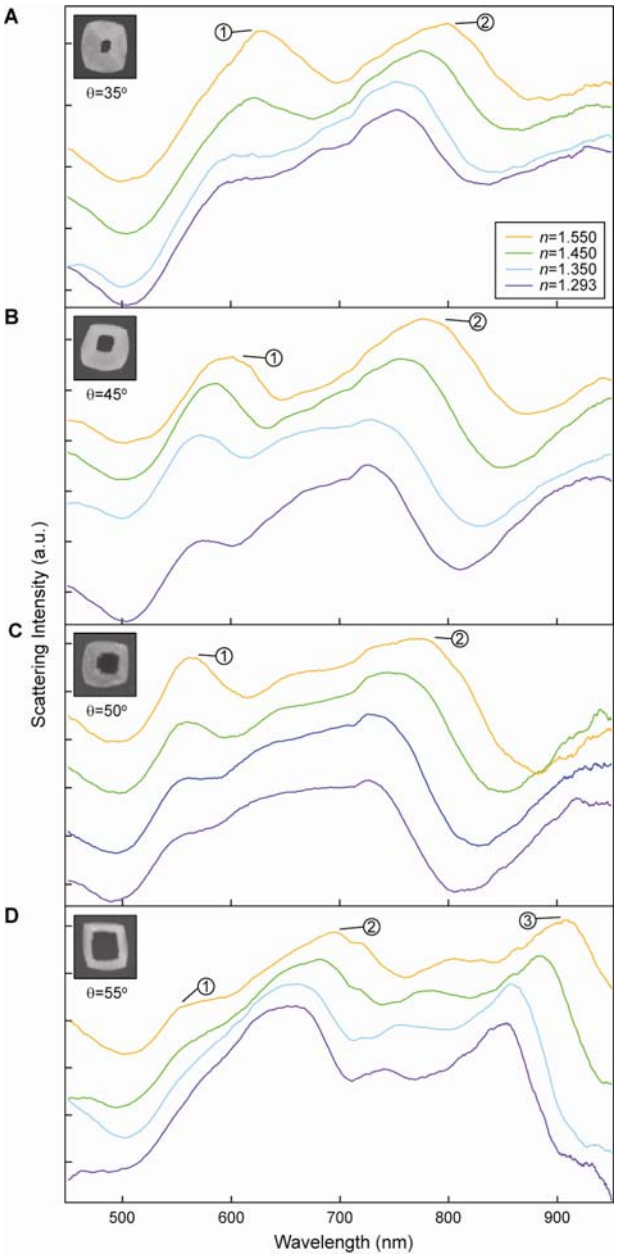

Figure 6.2.3.3. Sensitivity to dielectric environment study of TL and observed resonance shifts for θ=35, 45, 50, 55º.

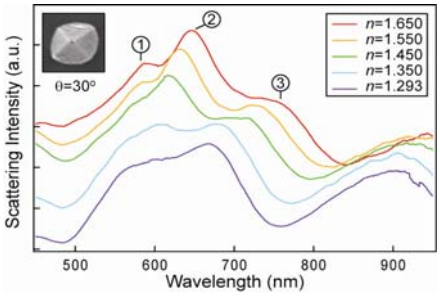

Figure 6.2.3.4. Sensitivity to dielectric environment study of square based WT and observed resonance

where $\Delta\lambda$ is the change in energy (eV), Δn is the change in refractive index units (RIU) and FWHM is the average of full width at half maximum (in eV). We observed that plasmon for resonances at lower wavelengths peak 1 (~550-600 nm) showed relatively low refractive index sensitivity (AVG=81 nm/RIU, over all particles) while the resonances at longer wavelength (peak 2, ~640-750 nm) demonstrated a higher degree of sensitivity (AVG=175 nm/RIU, over all particles). The TLs with θ=55° have a third resonance (peak 3) which occurs with in the visible region. The third resonance (~852-927 nm) demonstrated the highest sensitivity to refractive index changes (210 nm/RIU) (Figure 6.2.3.3).

When the shifts are calculated in eV, we find similarly high sensitivities. Table 6.2.3.1 summarizes the results of our refractive index studies for TPs with varying angles of deposition. The FOMs varied from 0.8-5.7. All spectra were converted to eV for FOM determination, where resonances were fit to a Gaussian to determine peak position and FWHM measurements. We found that the lower wavelength resonance (peak 1) exhibited less sensitivity to RI as the θ increased (148 nm/RIU for θ=35° and 42 nm/RIU for θ=55°). We hypothesize that this effect results from the TLs approaching the ideal case of the flat, thin ring. Such a structure would likely have a low FOM because it would be nearly two-dimensional. Complex structures (pyramids, rods, stars) tend to have higher FOM[32] than simpler structures (spheres) because localized field enhancements occur at sharp features in nanostructures.[30, 119, 123] This trend should hold true for TLs which have sharp corners as well. We examined all resonances to better understand trends and found that for TLs, as θ increased to 55° the FOM increased to 2.3 for the peak 2 resonances (~640-750 nm). The third resonance (peak 3) in the TL θ=55° spectra yields a FOM of 5.7 because of its higher sensitivity, 210 nm/RIU compared to 143 nm/RIU. We have

θ (°)	Δλ/RIU	FOM
30 (WT)	137 ±1.7 nm	1.6
35 (TL)	210 ±2.0 nm	1.7
45 (TL)	199 ± 5.8 nm	0.8
50 (TL)	190 ± 2.6 nm	1.3
55 (TL)	210 ± 1.8 nm	5.7

Table 6.2.3. Summarizes FOM and RI sensitivities observed for square based WT and TL pyramids.

observed the FOM increases with in deposition angle (θ) indicating that our thinner particles are more sensitive to changes in their dielectric environment. This behavior may signify an optimal deposition angle for high figures of merits based on a particular resonance feature.

6.3 Conclusions

This new extension of PEEL allows us to determine the relative contributions of the structural features of our complex particles. Our new method affords us an advantage over synthetic methods by allowing incremental structural changes that would be challenging or impossible in solution based synthesis. We have demonstrated a method to examine multipolar mixing of complex modes in TLs. This method allowed a systematic investigation of the contribution of one structural element (tip) to the LSP resonance of these particles. We found that the observed plasmon resonances experienced shifting to bluer wavelengths as the structures were progressively more truncated. Additionally, we discovered new resonances not found in circular base pyramids WT and attributed them to square base. This work has added to our knowledge of how architectural changes affect nanostructures optical properties and has enabled us to better design particles for specific uses such as photothermal therapy.[108]

References

1. Cui, Y.; Wei, Q.; Park, H.; Lieber, C. M., Nanowire sensors for Highly Sensitive and Selective Detection of Biological and Chemical Species. *Science* **2001,** 293, 1289-1292.
2. Kovtyukhova, N. I.; Martin, B. R.; Mbindyo, J. K. N.; Smith, P. A.; Razavi, B.; Mayer, T. S.; Mallouk, T. E., Layer-by-Layer Assembly of Rectifying Junctions in and on Metal Nanowires. *J. Phys. Chem. B.* **2001,** 105, 8762-8769.
3. Gudiksen, M. S.; Lauhon, L. J.; Wang, J.; Smith, D. C.; Lieber, C. M., Growth of nanowire superlattice structures for nanoscale photonics and electronics. *Nature* **2002,** 514, 617-620.
4. Huang, Y.; Duan, X.; Wei, Q.; Lieber, C. M., Directed Assembly of One-Dimensional Nanostructures into Functional Networks. *Science* **2001,** 291, 630-633.
5. Kim, F.; Kwan, S.; Akana, J.; Yang, P., Langmuir-Blodgett Nanorod Assembly. *J. Am. Chem. Soc.* **2001**, 43060-4361.
6. Duan, X.; Huang, Y.; Cui, Y.; Wang, J.; Leiber, C. M., Indium phosphide nanowires as building blocks for nanoscale electronic and optoelectronic devices. *Nature* **2001,** 409, 66-69.
7. Smith, A. S.; Nordquist, C. D.; Jackson, T. N.; Mayer, T. S.; Martin, B. R.; Mbindyo, J. K. N.; Mallouk, T. E., Electric-field assisted assembly and alignment of metallic nanowires. *Applied Physics Letters* **2000,** 77, 1399-1401.
8. Zhang, H.; Boussaad, S.; Ly, N.; Tao, N. J., Magnetic-field-assisted assembly of metal/polymer/metal junction sensors. *Appl. Phys. Lett.* **2004,** 84, 133-135.
9. Kuiry, S. C.; Patil, S. D.; Deshpande, S.; Seal, S., Spontaneous Self-Assembly of Cerium Oxide Nanoparticles to Nanorods through Supraaggregate Formation. *J. Phys. Chem. B.* **2005,** 109, 6936-6939.
10. Tang, Z.; Kotov, N. A.; Giersig, M., Spontaneous Organization of Single CdTe Nanoparticles into Luminescent Nanowires. *Science* **2002,** 297, 237-240.
11. Vlasov, Y. A.; Yao, N.; Norris, D. J., Synthesis of Photonic Crystals for Optical Wavelengths from Semiconductor Quantum Dots. *Advanced Materials* **1999,** 11, 165-169.
12. Yin, Y.; Lu, Y.; Gates, B.; Xia, Y., Template-Assisted Self-Assembly: A Practical Route to Complex Aggregates of Monodispersed Colloids with Well-Defined Sizes, Shapes, and Structures. *J. Am. Chem. Soc.* **2001,** 123, 8718-8729.
13. Donthu, S.; Pan, Z.; Myers, B.; Shekhawat, G.; Wu, N.; Dravid, V. P., Facile Scheme for Fabricating Solid-State Nanostructures Using E-Beam Lithography and Solution Precursors. *Nano Letters* **2005,** 5, (9), 1710-1715.
14. MoberlyChan, W. J.; Adams, D. P.; Aziz, M. J.; Hobler, G.; Schenkel, T., Fundementals of Focused Ion Beam Nanostructural Processing: Below, At and Above the Surface. *MRS Bulletin* **2007,** 32, 424-432.
15. Krauss, P. R.; Chou, S. Y., Fabrication of planar quantum magnetic disk structure using electron beam lithography, reactive ion etching, and chemical mechanical polishing. *J. Vac. Sci. Technol. B* **2005,** 13, 2850-2852.
16. Steffen, R.; Oshinowo, J.; Koch, T.; Forchel, A., InGaAs/GaAs quantum wires and dots defined by low-voltage electron-beam lithography. *J. Vac. Sci. Technol. B* **1995,** 13, 2888-2891.
17. Zhang, H.; Mirkin, C. A., DPN-Generated Nanostructures Made of Gold, Silver, and Palladium. *Chem. Mater.* **2004,** 16, 1480-1484.

18. Salaita, K.; Wang, Y.; Fragala, J.; Vega, R. A.; Liu, C.; Mirkin, C. A., Massively parallel dip-pen nanolithography with 55000-pen two-dimensional arrays. *Angewandte Chemie, International Edition* **2006,** 45, (43), 7220-7223.
19. Hulteen, J. C.; Duyne, R. P. V., Nanosphere lithography: A materials general fabrication process for periodic particle array surfaces. *J. Vac. Sci. Technol. B* **1995,** 13, 1553-1558.
20. Barton, J. E.; Odom, T. W., Mass-Limited Growth in Zeptoliter Beakers: A General Approach for the Synthesis of Nanocrystal. *Nano Letters* **2004,** 4, 1525-1528.
21. Odom, T. W.; Love, J. C.; Wolfe, D. B.; Paul, K. E.; Whitesides, G. M., Improved Pattern Transfer in Soft Lithography Using Composite Stamps. *Langmuir* **2002,** 18, 5314-5320.
22. Odom, T. W.; Thalladi, V. R.; Love, J. C.; Whitesides, G. M., Generation of 30-50 nm Structures Using Easily Fabricated, Composite PDMS Masks. *J. Am. Chem. Soc.* **2002,** 124, 12112-12113.
23. Sun, Y.; Khang, D. Y.; Hua, F.; Hurley, K.; Nuzzo, R. G.; Rogers, J. A., Photolithographic Route to the Fabrication of Micro/Nanowires of III-V Semiconductors. *Adv. Funct. Mater.* **2005,** 15, 30-40.
24. Yin, Y.; Gates, B.; Xia, Y., A Soft Lithography Approach to the Fabrication of Nanostructures of Single Crystalline Silicon with Well-Defined Dimensions and Shapes. *Adv. Mater.* **2000,** 12, 1426-1430.
25. Greyson, E. C.; Babayan, Y.; Odom, T. W., Directed Growth of Ordered Arrays of Small-Diameter ZnO Nanowires. *Adv. Mater.* **2004,** 16, 1348-1352.
26. Huang, M. H.; Mao, S.; Feich, H.; Yang, H.; Wu, Y.; Kind, H.; Weber, E.; Russo, R.; Yang, P., Room-Temperature Ultraviolet Nanowire Nanolasers. *Science* **2001,** 292, 1897-1899.
27. Kong, J.; Soh, H. T.; Cassell, A. M.; Quate, C. F.; Dai, H., Synthesis of Individual Single-Walled Carbon Nanotubes on Patterned Silicon Wafers. *Nature* **1998,** 395, 878-881.
28. Gopinath, A.; Boriskina, S. V.; Feng, N.-N.; Reinhard, B. M.; Negro, L. D., Photonic-Plasmonic Scattering Resonances in Deterministic Aperiodic Structures. *Nano Letters* **2008,** 8, (8), 2423-2431.
29. Guillaume, L.; Nordin, F.; Johan, G.; Jean, A.; Georges, L.; Andreas, H.; Franz, R. A.; Joachim, R. K., Raman scattering images and spectra of gold ring arrays. *Physical Review B (Condensed Matter and Materials Physics)* **2006,** 73, (24), 245417.
30. Henzie, J.; Shuford, K. L.; Kwak, E. S.; Schatz, G. C.; Odom, T. W., Manipulating the Optical Properties of Pyramidal Nanoparticle Arrays. *J. Phys. Chem. B* **2006,** 110, (29), 14028-14031.
31. Munechika, K.; Smith, J. M.; Chen, Y.; Ginger, D. S., Plasmon Line Widths of Single Silver Nanoprisms as a Function of Particle Size and Plasmon Peak Position. *The Journal of Physical Chemistry C* **2007,** 111, (51), 18906-18911.
32. Nehl, C. L.; Grady, N. K.; Goodrich, G. P.; Tam, F.; Halas, N. J.; Hafner, J. H., Scattering Spectra of Single Gold Nanoshells. *Nano Lett.* **2004,** 4, (12), 2355-2359.
33. Moulder, J. F.; Stickle, W. F.; Sobol, P. E.; Bomben, K. D., *Handbook of X-ray Photoelectron Spectroscopy*. Perkin-Elmer: 1992; p 259.
34. Williams, D. B.; Carter, C. B., *Transmission Electron Microscopy*. Plenum Press: New York and London, 1996; p 729.

35. Kelly, K. L.; Coronado, E.; Zhao, L. L.; Schatz, G. C., The Optical Properties of Metal Nanoparticles: The Influence of Size, Shape, and Dielectric Environment. *J. Phys. Chem. B* **2003,** 107, (3), 668-677.
36. Hasan, W.; Lee, J.; Henzie, J.; Odom, T. W., Selective Functionalization and Spectral Identification of Gold Nanopyramids. *J. Phys. Chem. C* **2007,** 111, (46), 17176-17179.
37. Ozbay, E., Plasmonics: Merging Photonics and Electronics at Nanoscale Dimensions. *Science* **2006,** 311, (5758), 189-193.
38. Stender, C. L.; Greyson, E. C.; Babayan, Y.; Odom, T. W., Patterned MoS_2 nanostructures over centimeter-square areas. *Advanced Materials* **2005,** 17, (23), 2837-+.
39. Zhang, H.; Loh, K. P.; Sow, C. H.; Gu, H.; Su, X.; Huang, C.; Chen, Z. K., Surface Modification Studies of Edge-Oriented Molybdenum Sulfide Nanosheets. *Langmuir* **2004,** 20, 6914-6920.
40. Barreau, N.; Bernede, J. C., MoS_2 textured films grown on glass substrages thourgh sodium sulfide based compounds. *J. Phys. D: Appl. Phys.* **2002,** 35, 1197-1204.
41. Ho, W.; Yu, J. C.; Lin, J.; Yu, J.; Li, P., Preparation and Photocatalytic Behavior of MoS2 and WS2 Nanocluster Sensitized TiO_2. *Langmuir* **2004,** 20, 5865-5869.
42. Kouzu, M.; Uchida, K.; Kuriki, Y.; Ikazaki, F., Micro-crystalline molybdenum sulfide prepared by mechanical milling as an unsupported model catalyst for hydrodesulfurization of diesel fuel. *Applied Catalysis A* **2004,** 276, 241-249.
43. Wilcoxon, J. P., Catalytic Photooxidation of Pentachlorophenol Using Semiconductor Nanoclusters. *J. Phys. Chem. B.* **2000,** 104, 7334-7343.
44. Loewenthal, S. H.; Chou, R. G.; Hopple, G. B.; Wenger, W. L., Evaluation of Ion Sputtered Moly Disulfide Bearings for Spacecraft Gimbals. *Tribology Transactions* **1994,** 37, 505-515.
45. Pavlov, I. M.; Shevakin, L. F.; Seidaliev, L. S., Use of molybdenum sulfide as a lubricant for cold rolling of tubes. *Wear* **1960,** 3, 406-407.
46. Singer, I. L.; Fayeulle, S.; Ehni, P. D., Wear behavior of triode-sputtered MoS_2 coatings in dry sliding contact with steel and ceramics. *Wear* **1996,** 195, 7-20.
47. Rapoport, L.; Bilik, Y.; Feldman, Y.; Homyonfer, M.; Cohen, S. R.; Tenne, R., Hollow Nanoparticles of WS_2 as Potential Solid-State Lubricants. *Nature* **1997,** 387, 791-793.
48. Li, Q.; Newbarg, J. T.; Walter, E. C.; Hemminger, J. C.; Penner, R. M., Polycrystalline Molybdenum Disulfide (2H-MoS_2) Nano- and Microribbons by Electrochemical/Chemical Synthesis. *Nano Letters* **2004,** 4, 277-281.
49. Li, Q.; Walter, E. C.; Veer, W. E. v. d.; Murrey, B. J.; Newberg, J. T.; Bohannan, E. W.; Switzer, J. A.; Hemminger, J. C.; Penner, R. M., Molybdenum Disulfide Nanowires and Nanoribbons by Electrochemical/Chemical Synthesis. *J. Phys. Chem. B.* **2005,** 109, 3169-3182.
50. Margulis, L.; Salitra, G.; Tenne, R.; Talianker, M., Nested fullerene-like structures. *Nature* **1993,** 365, 113-114.
51. Lee, H.; Kanai, M.; Kawai, T., Preperation of transition metal chalcogenide thin films by pulsed laser ablation. *Thin Solid Films* **1996,** 277, 98-100.
52. Ge, J.; Wang, J.; Zhang, H.; Li, Y., A General Atmospheric Pressure Chemical Vapor Deposition Synthesis and Crystallographic Study of Transition-Metal Sulfide One-Dimensional Nanostructures. *Chem. Eur. J.* **2004,** 10, 3525-3530.

53. Clark, A.; Williams, R. H., The optical properties of synthetic MoS_2. *Brit. J. Appl. Phys. (J. Phys. D.)* **1968,** 1, (2), 1222-1224.
54. Stender, C. L.; Odom, T. W., Chemical nanofabrication: a general route to surface-patterned and free-standing transition metal chalcogenide nanostructures. *J. Mater. Chem.* **2007,** 17, 1866-1869.
55. Olivas, A.; Cruz-Reyes, J.; Petranovskii, V.; Avalos, M.; Fuentes, S., Synthesis and characterization of nickel sulfide catalysts. *Journal of Vacuum Science & Technology A: Vacuum, Surfaces, and Films* **1998,** 16, (6), 3515-3520.
56. Rom, I.; Sitte, W., Composition dependent ionic and electronic conductivities and chemical diffusion coefficient of silver selenide at 160°C. *Solid State Ionics* **1997,** 101-103, (Part 1), 381.
57. Tenne, R., Inorganic nanotubes and fullerene-like nanoparticles. *J. Mater. Res.* **2006,** 21, (11), 2726-2743.
58. Rothschild, A.; Cohen, S. R.; Tenne, R., WS_2 nanotubes as tips in scanning probe microscopy. *Applied Physics Letters* **1999,** 75, (25), 4025.
59. Rapoport, L.; Fleischer, N.; Tenne, R., Applications of $WS_2(MoS_2)$ inorganic nanotubes and fullerene-like nanoparticles for solid lubrication and for structural nanocomposites. *J. Mater. Chem.* **2005,** 15, 1782-1788.
60. Henzie, J.; Barton, J. E.; Stender, C. L.; Odom, T. W., Large-area nanoscale patterning: chemistry meets fabrication. *Acc. Chem. Res.* **2006,** 39, (4), 249-257.
61. Terabe, K.; Hasegawa, T.; Nakayama, T.; Aono, M., Quantized conductance atomic switch. *Nature* **2005,** 433, (7021), 47-50.
62. Khang, D.-Y.; Jiang, H.; Huang, Y.; Rogers, J. A., A Stretchable Form of Single-Crystal Silicon for High-Performance Electronics on Rubber Substrates. *Science* **2006,** 311, (5758), 208-212.
63. Sun, Y.; Kim, H.; Menard, E.; Kim, S.; Adesida, I.; Rogers, J. A., Printed arrays of aligned GaAs wires for flexible transistors, diodes, and circuits on plastic substrates. *Small* **2006,** 2, (11), 1330-1334.
64. Jeong, U.; Camargo, P. H. C.; Lee, Y. H.; Xia, Y., Chemical transformation: a powerful route to metal chalcogenide nanowires. *Journal of Materials Chemistry* **2006,** 16, (40), 3893-3897.
65. Y. Babayan, J. E. B., E. C. Greyson, T. W. Odom, Templated and Hierarchical Assembly of CdSe/ZnS Quantum Dots. *Advanced Materials* **2004,** 16, (15), 1341-1345.
66. Hor, Y. S.; Xiao, Z. L.; Welp, U.; Ito, Y.; Mitchell, J. F.; Cook, R. E.; Kwok, W. K.; Crabtree, G. W., Nanowires and Nanoribbons of Charge-Density-Wave Conductor NbSe3. *Nano Letters* **2005,** 5, (2), 397-401.
67. Mane, R. S.; Lokhande, C. D., Chemical deposition method for metal chalcogenide thin films. *Materials Chemistry and Physics* **2000,** 65, (1), 1.
68. Sharma, S. K.; Kumar, S.; Kumar, V.; Sharma, T. P., CdSe photovoltaic sintered films. *Opt. Mater.* **1999,** 13, 261-265.
69. Solorza-Feria, O.; Ellmer, K.; Giersig, M.; Alonso-Vante, N., Novel low-temperature synthesis of semiconducting transition metal chalcogenide electrocatalyst for multielectron charge transfer: molecular oxygen reduction. *Electrochim. Acta* **1994,** 39, (11-12), 1647-1653.

70. Rapoport, L.; Leshchinsky, V.; Volovik, Y.; Lvovsky, M.; Nepomnyashchy, O.; Feldman, Y.; Popovitz-Biro, R.; Tenne, R., Modification of contact surfaces by fullerene-like solid lubricant nanoparticles. *Surface and Coatings Technology* **2003,** 163-164, 405.
71. Liang, C.; Terabe, K.; Hasegawa, T.; Aono, M., Template synthesis of M/M_2S (M = Ag, Cu) hetero-nanowires by electrochemical technique. *Solid State Ionics* **2006,** 177, (26-32), 2527.
72. Moses, P. G.; Hinnemann, B.; Topsoe, H.; Norskov, J. K., The hydrogenation and direct desulfurization reaction pathway in thiophene hydrodesulfurization over MoS_2 catalysts at realistic conditions: A density functional study. *Journal of Catalysis* **2007,** 248, (2), 188.
73. Dominko, R.; Gaberscek, M.; Arcon, D.; Mrzel, A.; Remskar, M.; Mihailovic, D.; Pejovnik, S.; Jamnik, J., Electrochemical preparation and characterization of Li_zMoS_{2-x} nanotubes. *Electrochim. Acta* **2003,** 48, 3079-3084.
74. Nath, M.; Rao, C. N. R., Nanotubes of the disulfides of group 4 and 5 metals. *Pure Appl. Chem.* **2002,** 74, (9), 1545-1552.
75. Chhowalla, M.; Amaratunga, G., Thin films of fullerene-like MoS_2 nanoparticles with ultra-low friction and wear. *Nature* **2000,** 407, 164-167.
76. Falk, A.; Deshmukh, M. M.; Prieto, A. L.; Urban, J. J.; Jonas, A.; Park, H., Magnetic switching of phase-slip dissipation in $NbSe_2$ nanoribbons. *Phys. Rev. B: Condens. Matter Mater. Phys.* **2007,** 75, 020501.
77. Laiho, R.; Safonchik, M.; Traito, K. B., Quasiclassical approach to nonlocal generalized London equation in mixed state of s-wave superconductors. *Physical Review B* **2007,** 75, 174524-1-6.
78. Xingcai, W.; Yourong, T.; Yeming, H.; Song, Y.; Zheng, H.; Jungjie, Z.; Dong, L., Tantalum disulfide nanobelts: preparation, superconductivity and field emission *Nanotechnology* **2006,** 17, 201-205.
79. Zhou, Z.; Jin, R.; Eres, G.; Mandrus, D.; Barzykin, V.; Schlottmann, P.; Hor, Y. S.; Xiao, Z.; Mitchell, J. F., Resistance and current-voltage characteristics of individual superconducting $NbSe_2$ nanowires. *Phys. Rev. B: Condens. Matter Mater. Phys.* **2007,** 76, (10), 104511.
80. Frindt, R. F., Superconductivity in Ultrathin NbSe2 Layers. *Physical Review Letters* **1972,** 28, (5), 299.
81. Nath, M.; Kar, S.; Raychaudhuri, A. K.; Rao, C. N. R., Superconducting NbSe2 nanostructures. *Chemical Physics Letters* **2003,** 368, (5-6), 690-695.
82. Dunnill, C. W.; Edwards, H. K.; Brown, P. D.; Gregory, D. H., Single-Step Synthesis and Surface-Assisted Growth of Superconducting TaS_2 Nanowires. *Angewandte Chemie International Edition* **2006,** 45, (42), 7060-7063.
83. Orlov, A. P.; Latyshev, Y. I.; Smolovich, A. M.; Monceau, P., Interaction of both charge density waves in $NbSe_3$ from interlayer tunneling experiments. *JETP Letters* **2006,** 84, (2), 89-92.
84. Pokrovskii, V., Ya.; Zybtsev, S., G.; Gorlova, I., G., Torsional Strain of TaS_3 Whiskers on the Charge-Density Wave Depinning. *Phys. Rev. Lett.* **2007,** 98, 206404-1-4.
85. Toshima, T.; Tanda, S., Synthesizing nanocrystals of metal di-chalcogenide charge density wave system. *Physica C: Superconductivity* **2005,** 426-431, (Part 1), 426-430.
86. Slot, E.; Holst, M. A.; van der Zant, H. S. J.; Zaitsev-Zotov, S. V., One-Dimensional Conduction in Charge-Density-Wave Nanowires. *Physical Review Letters* **2004,** 93, (17), 176602.

87. Zaitsev-Zotov, S., V.; Minakova, V., E., Evidence of Collective Transport in the Ohmic Regime of *o*-TaS_3 in the Charge-Density-Wave State by a Photoconduction Study. *Physical Review Letters* **2006,** 97, 266404-1-4.
88. Hor, Y. S.; Welp, U.; Ito, Y.; Xiao, Z. L.; Patel, U.; Mitchell, J. F.; Kwok, W. K.; Crabtree, G. W., Superconducting $NbSe_2$ nanowires and nanoribbons converted from $NbSe_3$ nanostructures. *Applied Physics Letters* **2005,** 87, (14), N.PAG.
89. Toshima, T.; Inagaki, K.; Hatakenaka, N.; Tanda, S., Supercluster of Electrons in Ultrathin $TaSe_2$ Nanocrystals. *J. Phys. Soc. Jpn.* **2006,** 75, 24706-1-24706-5.
90. Zhixian, Z.; Rongying, J.; Gyula, E.; David, M.; Victor, B.; Pedro, S.; Yew-San, H.; Zhili, X.; John, F. M., Resistance and current-voltage characteristics of individual superconducting $NbSe_2$ nanowires. *Physical Review B (Condensed Matter and Materials Physics)* **2007,** 76, (10), 104511.
91. Duphil, D.; Bastide, S.; Rouchaud, J. C.; Pastol, J. L.; Legendre, B.; Levy-Clement, C., The chemical synthesis in solution and characterization of transition metal dichalcogenides MX_2 (M=Mo, W; X=S, Se) nanoparticles. *nanotechnol.* **2004,** 15, 828-832.
92. Cao, X.; Lu, Q.; Xu, X.; Yan, J.; Zeng, H., Single-crystal snowflake of Cu_7S_4: Low temperature, large scale synthesis and growth mechanism. *Materials Letters* **2008,** 62, (17-18), 2567-2570.
93. Nan, Z.; Wang, X.-Y.; Zhao, Z., Formation of various morphologies of copper sulfides by a solvothermal method. *Journal of Crystal Growth* **2006,** 295, (1), 92-96.
94. Subhajit, B.; Soumitra, K., Fabrication of ZnS nanoparticles and nanorods with cubic and hexagonal crystal structures: a simple solvothermal approach. *Nanotechnology* **2008**, (4), 045710.
95. Wang, X.; Wan, F.; Gao, Y.; Liu, J.; Jiang, K., Synthesis of high-quality Ni_2P hollow sphere via a template-free surfactant-assisted solvothermal route. *Journal of Crystal Growth* **2008,** 310, (10), 2569-2574.
96. Jana, S.; Baek, I. C.; Lim, M. A.; Seok, S. I., ZnSe colloidal nanoparticles synthesized by solvothermal method in the presence of $ZrCl_4$. *Journal of Colloid and Interface Science* **2008,** 322, (2), 473-477.
97. Li, Q.; Ding, Y.; Liu, X.; Qian, Y., Preparation of ternary I-IV-VI nanocrystallines via a mild solution route. *Materials Research Bulletin* **2001,** 36, (15), 2649-2656.
98. Xie, Y.; Su, H.; Li, B.; Qian, Y., A direct solvothermal route to nanocrystalline selenides at low temperature. *Materials Research Bulletin* **2000,** 35, (3), 459-464.
99. Yang, J.; Cheng, G. H.; Zeng, J. H.; Yu, S. H.; Liu, X. M.; Qian, Y. T., Shape Control and Characterization of Transition Metal Diselenides MSe_2 (M = Ni, Co, Fe) Prepared by a Solvothermal-Reduction Process. *Chem. Mater.* **2001,** 13, (3), 848-853.
100. Feldman, Y.; Frey, G. L.; Homyonfer, M.; Lyakhovitskaya, V.; Margolin, A.; Cohen, S. R.; Hodes, G.; Hutchison, J. L.; Tenne, R., Bulk Synthesis of Inorganic Fullerene-like MS_2 (M=Mo, W) from the Respective Trioxides and the Reaction Mechanism. *J. Am. Chem. Soc.* **1996,** 118, (5362-5367).
101. Manashi, N.; Rao, C. N. R., New Metal Disulfide Nanotubes. *J. Am. Chem. Soc.* **2001,** 123, 4841-4842.
102. Margolin, A.; Popovitz-Biro, R.; Alby-Yaron, A.; Rapoport, L.; Tenne, R., Inorganic fullerene-like nanoparticles of TiS_2. *Chem. Phys. Lett.* **2005,** 411, 162-166.

103. Rao, C. N. R., Chemical Routes to Nanocrystals, Nanowires and Nanotubes. *Int. J. Nanosci.* **2005,** 4, (5,6), 811-826.
104. Schuffenhauer, C.; Popovitz-Biro, R.; Tenne, R., Synthesis of NbS_2 nanoparticles with (nested) fullerene-like structure (*IF*). *J. Mater. Chem.* **2002,** 12, 1587-1591.
105. Barton, J. E.; Stender, C. L.; Pheobe, L.; Odom, T. W., Synthesis and Structural Control of Anodic Ta_2O_5 Nanotubes. *In Process* **In Process**.
106. Chamberlin, D. R.; Wang, Z.; Sultana, K. A.; Chow, E. K.; Sigalas, M. M.; Liu, M.; Grot, A. C.; Fan, S. In *SERS and plasmon resonance of engineered nanoparticle arrays*, 2005; Mark, I. S., Ed. SPIE: 2005; p 592708.
107. Henzie, J.; Lee, M. H.; Odom, T. W., Multiscale patterning of plasmonic metamaterials. *Nat Nano* **2007,** 2, (9), 549.
108. Hasan, W.; Stender, C. L.; Lee, M. H.; Nehl, C.; Lee, J.; Odom, T. W., Tailoring the Surface Plasmon Resonance of Nanopyramids for Optical Heat Generation. *NanoLetters*, **Submitted**.
109. Huang, X.; El-Sayed, I. H.; Qian, W.; El-Sayed, M. A., Cancer Cell Imaging and Photothermal Therapy in the Near-Infrared Region by Using Gold Nanorods. *J. Am. Chem. Soc.* **2006,** 128, (6), 2115-2120.
110. Lin, A. W. H.; Lewinski, N. A.; Rakalin, A. A.; Lee, M.; Halas, N. J.; Drezek, R. A., Modeling and experimental observations of gold nanoshell reflectance. *Proc. of SPIE* **2005,** 6010, 60100L-1-60100L-8.
111. Xiong, Y.; Wiley, B. J.; Xia, Y., Nanocrystals with Unconventional Shapes - A Class of Promising Catalysts. *Angewandte Chemie International Edition* **2007,** 46, (38), 7157-7159.
112. Orendorff, C. J.; Murphy, C. J., Quantitation of Metal Content in the Silver-Assisted Growth of Gold Nanorods. *J. Phys. Chem. B* **2006,** 110, (9), 3990-3994.
113. Orendorff, C. J.; Gearheart, L.; Jana, N. R.; Murphy, C. J., Aspect ratio dependence on surface enhanced Raman scattering using silver and gold nanorod substrates. *Physical Chemistry Chemical Physics* **2006,** 8, 165-170.
114. Sau, T. K.; Murphy, C. J., Room Temperature, High-Yield Synthesis of Multiple Shapes of Gold Nanoparticles in Aqueous Solution. *J. Am. Chem. Soc.* **2004,** 126, (28), 8648-8649.
115. Xue, C.; Mirkin, C. A., pH-Switchable Silver Nanoprism Growth Pathways. *Angewandte Chemie International Edition* **2007,** 46, (12), 2036-2038.
116. Xia, Y.; Halas, N., Shape-controlled synthesis and surface surface plasmonic properties of metallic nanostructures. *MRS Bulletin* **2005,** 30, (5), 338-348.
117. Stiles, P. L.; Dieringer, J. A.; Shah, N. C.; Van Duyne, R. P., Surface-Enhanced Raman Spectroscopy. *Annual Review of Analytical Chemistry* **2008,** 1, (1), 601-626.
118. Burgin, J.; Langot, P.; Del Fatti, N.; Valle 靄 e, F.; Huang, W.; El-Sayed, M. A., Time-Resolved Investigation of the Acoustic Vibration of a Single Gold Nanoprism Pair. *The Journal of Physical Chemistry C* **2008,** 112, (30), 11231-11235.
119. Lu, Y.; Liu, G. L.; Kim, J.; Mejia, Y. X.; Lee, L. P., Nanophotonic Crescent Moon Structures with Sharp Edge for Ultrasensitive Biomolecular Detection by Local Electromagnetic Field Enhancement Effect. *Nano Lett.* **2005,** 5, (1), 119-124.
120. Bukasov, R.; Shumaker-Parry, J. S., Highly Tunable Infrared Extinction Properties of Gold Nanocrescents. *Nano Letters* **2007,** 7, (5), 1113-1118.

121. Shuford, K. L.; Lee, J.; Odom, T. W.; Schatz, G. C., Optical Properties of Gold Pyramidal Shells. *J. Phys. Chem. C* **2008,** 112, (17), 6662-6666.
122. Lee, J.; Hasan, W.; Stender, C. L.; Odom, T. W., Pyramids: A Platform for Designing Multifunctional Plasmonic Particles. *Acc. Chem. Res.* **2008**.
123. Sherry, L. J.; Chang, S. H.; Schatz, G. C.; VanDuyne, R. P.; Wiley, B. J.; Xia, Y., Localized Surface Plasmon Resonance Spectroscopy of Single Silver Nanocubes. *Nano Lett.* **2005,** 5, (10), 2034-2038.
124. Geohegan, D. B.; Puretzky, A. A., Dynamics of laser ablation plume penetration through low pressure background gases. *Applied Physics Letters* **1995,** 67, 197-199.
125. Kokai, F.; Takahashi, K.; Yudasaka, M.; Iijima, S., Emission Imaging Spectroscopic and Shadowgraphic Studies on the Growth Dynamics of Graphitic Carbon Particles Synthesized by CO_2 Laser Vaporization. *The Journal of Physical Chemistry B* **1999,** 103, (41), 8686-8693.
126. Yudasaka, M.; Ichihashi, T.; Iijima, S., Roles of Laser Light and Heat in Formation of Single-Wall Carbon Nanotubes by Pulsed Laser Ablation of $C_xNi_yCo_y$ Targets at High Temperature. *The Journal of Physical Chemistry B* **1998,** 102, (50), 10201-10207.

Appendix 1

LA/CVD Furnace Construction

LA-assisted growth is a useful synthetic technique owing to the generation of clean, highly crystalline nanostructures.[51, 124] The target materials are usually doped with transition metals that act as catalytic seed particles and thus facilitate the growth of nanostructures as the ablated material cools.[125, 126] Figure A1 provides a schematic diagram of the system we built. While many different pulsed laser sources can be used in laser ablation (Nd:YAG, CO_2, Eximer), a 20 ns pulsed KrF eximer laser was chosen for our source because of its tunable output, adjustable repetition rate, and flexibility for uses with other on going projects. Because the laser pulse source can degrade the integrity of the target overtime, we designed an electronically controllable mirror system that can scan the beam across the target surface during ablation (Figure A1A). To make the CVD compatible with corrosive precursor materials, we selected all stainless steel parts and fitting (Figure A1B). For flexibility in controlling the flow rates of the precursor and inert gases, mass flow controllers (MFCs) with different flow rates were selected (Figure A1C) (20-1000 sccm). MFCs are computer-controlled valves that allow for precise monitoring and control of the gas flow rates. The highest flow rate MFC is usually reserved for the inert carrier gas and the lowest for toxic gases. The carrier gas can be thought of as the "solvent" for a gas phase reaction and all other gases as "reagents." VCR fittings were chosen because they provide an excellent seal against gas leaks and can be taken apart easily for instrument modification or maintenance, unlike standard ferrule fittings. The system operation is controlled by a computer, which allows precise control over the amounts of gas in the reaction gas mixture in order to optimize reaction conditions. A vacuum pump on the system outlet allows for pressure control and method to purge the system of excess oxygen (Figure A1D).

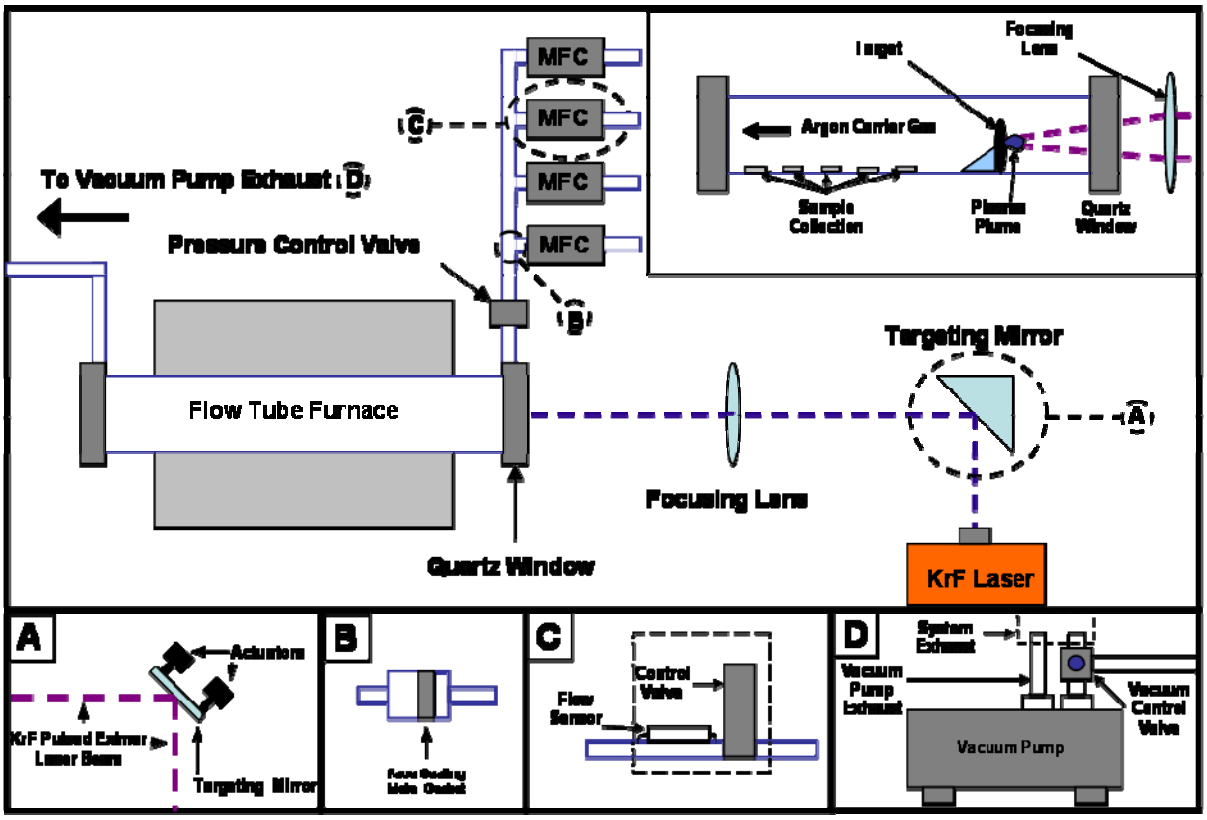

Figure A1. Diagram of LA/CVD

Appendix 2

Tilting Rotating Stage Construction

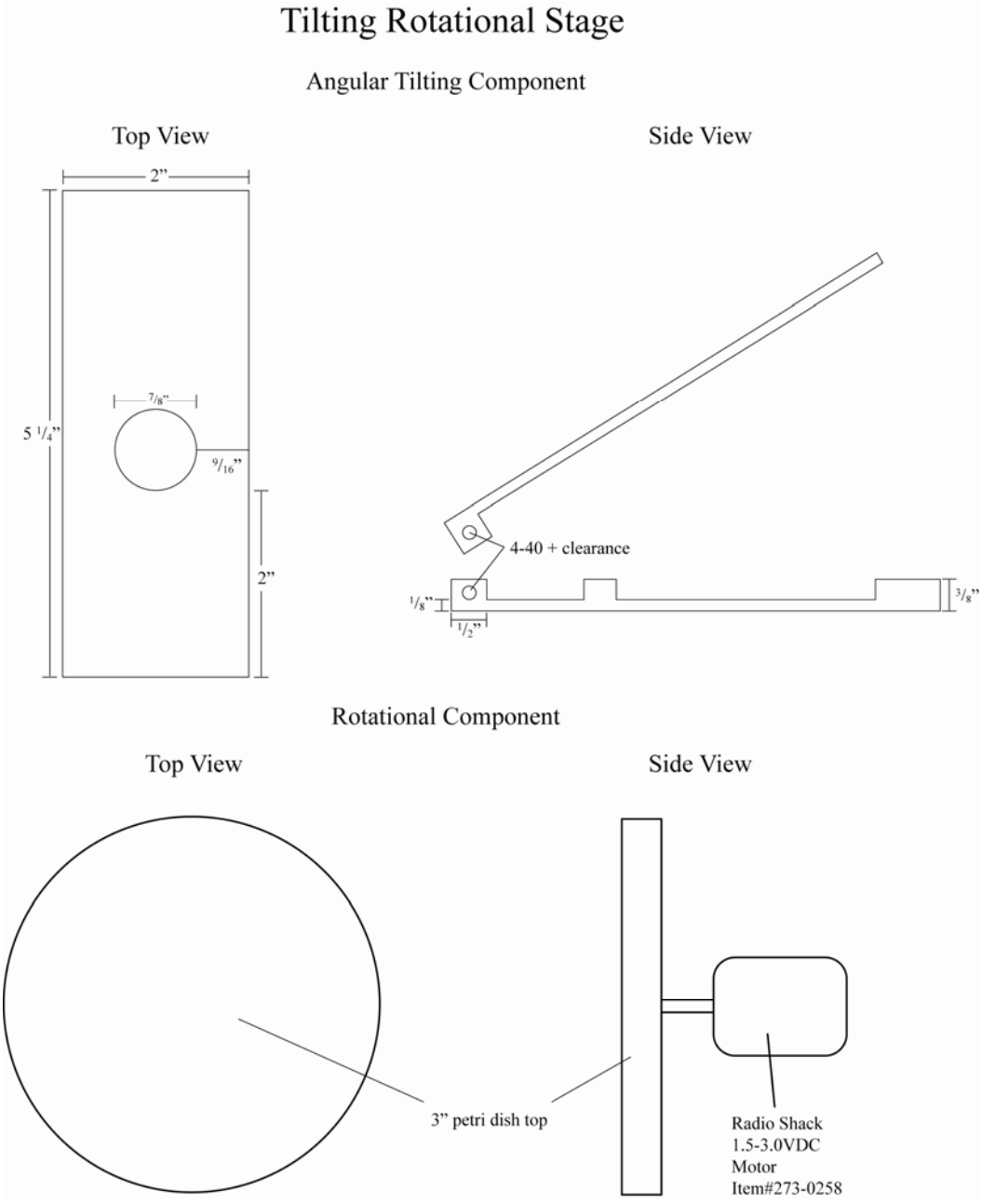

Figure A2: Diagram of Tilting Rotational Stage